Energy & Environmental Science

Dynamic Article Links

Cite this: *Energy Environ. Sci.*, 2012, **5**, 5619

www.rsc.org/ees

PERSPECTIVE

Highly porous chemically modified carbon cryogels and their coherent nanocomposites for energy applications

Stephanie L. Candelaria,[a] Rong Chen,[bc] Yoon-Ha Jeong[d] and Guozhong Cao*[a]

Received 9th September 2011, Accepted 27th October 2011
DOI: 10.1039/c1ee02634h

Highly porous carbon cryogels with tunable pore structure and chemical composition were synthesized through controlled hydrolysis and polycondensation reactions using different chemicals as precursors and either NaOH or hexamine ($C_6N_{12}N_4$) as catalysts. Gelation was followed with freeze drying to preserve the highly porous structure during solvent removal and controlled pyrolysis of the organic hydrogels and subsequent optional activation was performed. In addition, two different approaches were taken to modify the surface chemistry of porous carbon to introduce nitrogen or nitrogen-boron, leading to different porous structures and surface chemistry, as well as electrochemical properties. These carbon cryogels have been characterized and studied for energy storage applications. Specifically, they have been investigated as electrodes for electric double layer supercapacitors, high energy and high power density lithium-ion batteries with vanadium pentoxide deposited inside the pores, porous media for natural gas (methane) storage at reduced pressure, and scaffolds for hydride nanocomposites for greatly improved hydrogen storage. The relationship between processing conditions, chemical composition, pore structure, and energy storage properties are discussed.

1. Introduction

Carbon assumes an array of structural forms, such as diamond, graphite, graphene, fullerenes, carbon nanotubes, and amorphous carbon.[1,2] The latter can be further divided into diamond-like carbon and graphitic carbon. The difference between these two forms of amorphous carbon lies in their respective molecular orbital hybridization: diamond-like carbon has sp^3 hybridization, while graphitic carbon has sp^2 hybridization. Both diamond and diamond-like carbon possess excellent mechanical properties, optical properties, and thermal conductivity. This is largely due to the small size and close packing of carbon atoms, as well as short and strong chemical bonds between these atoms. Graphite and graphitic carbons, on the other hand, are excellent electrical conductors. Graphene, carbon nanotubes, and fullerenes are all derivatives of graphite and have attracted significant attention lately in the research community, partly due to their unique and technically important physical properties.

Arguably, carbon is one of the elements most intimately associated with current energy and environmental issues. Modern society is built upon cars, airplanes, computers, and portable electronics, just to name a few. All these rely on the continued supply of energy either in the form of gasoline or electricity, which is generated mainly from fossil fuels such as

[a]*Department of Materials Science and Engineering, University of Washington, Seattle, WA, USA*
[b]*Intel Labs, Santa Clara, CA, USA*
[c]*State Key Lab of Digital Manufacturing Equipment & Technology, School of Mechanical Science and Engineering, Huazhong University of Science & Technology, Wuhan, 430074, China*
[d]*National Center for Nanomaterials Technology, Pohang University of Science and Technology, Pohang, South Korea*

Broader context

Modern society relies heavily on fossil fuels, but over the past several years there has been an increased demand for the development of alternative energy technologies that are clean and sustainable. Significant progress has been made to make these more practical and cost competitive, and carbon materials are playing a significant role in this. In this perspective article, a number of alternative energy applications for porous carbon are discussed, including electric double layer supercapacitors, high energy and high power density lithium-ion batteries with vanadium pentoxide deposited inside the pores, porous media for natural gas (methane) storage at reduced pressure, and scaffolds for hydride nanocomposites for greatly improved hydrogen storage. The ability to tune both porous structure and surface chemistry gives rise to enhanced energy storage capacity when used in supercapacitors and lithium ion batteries, as well as tunable dehydrogenation temperature for gas storage.

coal and oil. Over the past several decades, significant progress has been made in an effort to develop alternative technologies to harvest and use clean, sustainable energy including solar energy, wind power, biofuels, and hydrogen, as well as clean energy technologies, such as fuel cells and lithium ion batteries. Although these types of energy sources have been marginalized in the past, new technology is making alternative energy more practical and often price competitive with fossil fuels, and it is expected that the coming decades will usher in a long expected transition away from coal and oil as our primary fuel.

Carbon materials have been playing a significant role in the development of alternate clean and sustainable energy technologies. For example, fullerene-containing p-type semiconducting polymers are one of the key foundations in rapidly advancing organic photovoltaics.[3–6] Additionally, carbon nanotubes and graphenes are being investigated as critical additives for the next generation of optically transparent electronically conductive films for solar cells.[7–9] Carbon nanotubes and graphenes are also studied for the development of batteries and supercapacitors.[10–17]

Highly porous carbon has been widely used as filters, sorbents, scaffolds, and matrices in many technically important fields. Examples include water purification,[18–20] artificial livers or kidneys,[21–24] and catalyst support,[25–28] among others. Highly porous carbon can be divided into two groups: (1) derived from naturally occurring carbonaceous precursors such as coal, wood, coconut shells, fruit stones, and other agricultural byproducts,[29–33] and (2) synthetic porous carbon.[34–37] There are a number of ways to synthesize porous carbon, examples of which include sol–gel processing,[38–40] etching of metal carbides,[41–43] and templated carbon.[44–47] Our research focused on the synthesis of porous carbon through sol–gel processing of highly organic gel, followed with aging, solvent exchange, solvent removal using freeze-drying, and then pyrolysis to convert the porous organic gel to porous carbon gel.

Sol–gel processing[48,49] is one of the most widely used methods, also often combined with hydrothermal growth, to prepare various nanostructured materials and films,[50] such as those used in the new dye sensitized solar cells.[51,52] Sol–gel processing is a solution method of making hydrogels (*i.e.*, a solid skeleton filled with solvent) for metal oxides, organic-inorganic hybrids, and polymers from various precursors (including alkoxides, salts, and organic monomers) through controlled hydrolysis and condensation.[48,49] For example, TiO_2 nanoparticles and films can be obtained by reacting titanium isopropyl oxide with water, followed with hydrothermal growth. The crystallinity, particle sizes, pore structure, surface area, and degree of agglomeration depend on the reaction conditions, including the temperature, evaporation rate, drying conditions, and post-treatments. The rate of hydrolysis and condensation is largely affected by the type of precursors, the acid and base concentrations, and the mixture of solvents (*e.g.* water *vs.* other solvents). The advantage of the sol–gel approach is the flexibility of the sol–gel chemistry and the wide range of microstructures that can be attained, from nanostructured highly porous films or monoliths to nanoparticles. To preserve the highly open and porous structure, supercritical drying is commonly applied for the removal of solvent.[53,54] During supercritical drying, there exists no liquid–vapor interface and thus no capillary force; as a result there is no capillary force driven collapse or shrinkage of the highly open gel network. Such synthesized sol–gel materials are referred to as aerogels, which are highly porous with porosity up to 99.9% and specific surface area exceeding 1000 $m^2\ g^{-1}$. Freeze-drying is less widely applied in sol–gel research.[36] In a typical freeze-drying process, the hydrogels are first frozen and then the pressure is reduced to allow the frozen water or solvent to sublime directly from the solid phase to the gas phase. Similar to supercritical drying, there will be no capillary force developed during the removal of solvent, so that the highly porous structure is retained. The freeze-dried gels are referred to as cryogels. Aerogels and cryogels are similar: both highly porous with high specific surface area.[55–58]

There have been some excellent perspective articles and reviews published lately discussing the recent progress in the development of porous carbon and its energy related applications.[59,55,60–62] This perspective article focuses on summarizing and reviewing our recent work on the synthesis and surface modification of highly porous carbon through a combination of sol–gel processing, freeze-drying, and subsequent pyrolysis for energy storage applications: (1) electrodes for electrostatic double layer capacitors (EDLCs), (2) scaffolds to synthesize vanadium pentoxide nanocomposites for cathodes in lithium-ion batteries, (3) porous media for methane gas storage, and (4)

Stephanie L. Candelaria

Stephanie L. Candelaria is pursuing a Ph.D. in the Department of Materials Science and Engineering at the University of Washington under the direction of Professor Guozhong Cao. Her current research is focused on the sol–gel processing and electrochemical characterization of highly porous carbon from renewable resources for supercapacitors.

Guozhong Cao

Dr Guozhong Cao is Boeing-Steiner Professor of Materials Science and Engineering, Professor of Chemical Engineering, and Adjunct Professor of Mechanical Engineering at the University of Washington. He has published over 280 papers, 7 books, and 4 proceedings. His recent research is focused mainly on solar cells, lithium-ion batteries, supercapacitors, and hydrogen storage.

matrices to form coherent nanocomposites with ammonia borane for hydrogen storage. The relationships between precursors, catalysts, processing conditions, nano- and microstructures, and properties for energy storage applications will be discussed.

2. Fabrication of porous carbon

Typically, carbon cryogels are made in a three-step process. First, hydrogels are synthesized by sol–gel polycondensation of organic monomers, such as resorcinol and formaldehyde, in an aqueous solution in the presence of a polymerization catalyst.[34,35,37,55,63,64] Subsequently, the resulting hydrogels are dried by freeze drying, at which point they are referred to as organic cryogels. Finally, carbon cryogels are produced by pyrolysis of organic cryogels at elevated temperatures in nitrogen. They can be activated to further increase the porosity and specific surface area and tune the porous structure to meet various application requirements. Carbon cryogels presented in this paper were synthesized from various monomer precursors with different catalysts, and the chemistry or surface chemistry of carbon cryogels were tuned through either incorporating pre-selected precursors during the hydrolysis-polymerization process or impregnating the pores of either hydrogels prior to the removal of solvent or carbon cryogels after solvent removal, pyrolysis, and activation.

Two different types of porous carbon were synthesized with different chemical precursors: one is carbon cryogels from resorcinol ($C_6H_6O_2$), formaldehyde (CH_2O), and a metal ion catalyst, and another is nitrogen-containing carbon cryogels from resorcinol, furaldehyde ($C_5H_4O_2$), and a reactive catalyst, hexamine ($C_6N_{12}N_4$). In addition, two different approaches were taken to modify the surface chemistry of porous carbon. One is to introduce boron and nitrogen to the surface of porous carbon through impregnating hydrogels with ammonia borane *via* solvent exchange prior to freeze drying and pyrolysis. Another is to introduce nitrogen alone to the surface of porous carbon through sublimation of hexamine after the pyrolysis and activation of hydrogels. The porous structure, chemical composition of the carbon skeleton, and the surface chemistry of the resulting porous carbon cryogels are appreciably different from one another.

The first type of carbon cryogels (CCs) were prepared using the resorcinol and formaldehyde polycondensation process with sodium carbonate as a catalyst, initially published by Pekala.[34,35] Gelation was followed by freeze drying and pyrolysis in N_2 and then activation in CO_2. The variation in the pore structure of the samples was achieved chemically by altering the amount of catalyst used and the degree of CO_2 activation.

CCs fabricated are all glassy carbons when pyrolyzed, which are known to possess a graphite-like structure or graphene ribbons that have a short-range crystalline arrangement but lack a long-range crystalline structure.[2] Non-Resonant X-ray Raman spectrum (XRS) data support this characteristic of the cryogels. The CC samples all had the same XRS as shown in Fig. 1, regardless the chemical precursors, processing conditions, pyrolysis and activation temperature and time.[65] The samples are highly defective or have large amounts of dangling bonds and have a longer C–C bond length. All carbons are sp^2 hybridized, which accounts for their good conductivity.[66] From a structural point of view, the most important aspects derived from the XRS analysis are their short-range order, amorphous structure, and the high number of dangling bonds. During activation these aspects of the CCs are responsible for producing selective regions where it is possible for new microporosity to be generated.[67]

For porous carbon, the two most important structural parameters are the surface area and the pore size. Using distributions calculated with the Dubinin-Astakhov (DA) and Barrett-Joyner-Halenda (BJH) methods, the pore size of the samples can be categorized between those produced during micropore filling ($P/P_0 < 0.1$) and capillary condensation, or mesopore filling ($P/P_0 > 0.3$).[69–71] The porous structure of carbon cryogels can be tuned by various processing parameters. For example, two samples with the same composition, C-36 and C-70, but with different levels of activation, were prepared. The resorcinol to catalyst (R/C) ratio was set to 75 and C-36 was activated to 36% while C-70 was activated to 70%. Both exhibit similar pore size while having varying pore volume and surface area.[67,72,73] This is seen in the nitrogen sorption isotherms of the two samples, which have the same shape, but differ in the adsorbed volume (as shown in Fig. 2). The pore size distributions of C-36 and C-70 extend from 1.2 nm in the DA distribution until vanishing around 10 nm in the BJH distribution. Another sample, A-70, was prepared with an R/C ratio of 25 and an activation level of 70%. When compared to C-70, they demonstrated different pore size distributions, as well as different pore volumes and specific surface area. A-70 had mostly pores in the micropore region (80%), in contrast to only 57% micropores in C-70. In addition, the pore size distribution was narrower, from 1.62 nm and covering a similar extent to C-36 and C-70 in the mesopore region, as seen in Fig. 2b.

The second type of porous carbon cryogels were prepared using the monomers resorcinol, furaldehyde, and hexamethylenetetramine (HMTA or hexamine), $C_6H_{12}N_4$, as an amine base catalyst. A similar synthesis process was developed by Wu *et al.*[37] However, this new synthesis used the solvent's chemistry and pH, *i.e.* the polycondensation reaction took place in solvent mixtures of *tert*-butanol and water.[74] With resorcinol and furaldehyde as precursors, the polymerization reactions take place in an organic solvent directly, thus the wet gels are ready for solvent removal by either supercritical, ambient, or freeze drying[75,37] without the need for solvent exchange. This polycondensation reaction is more complex, in which functional groups from the catalyst decomposition enhance the gels structural properties in addition

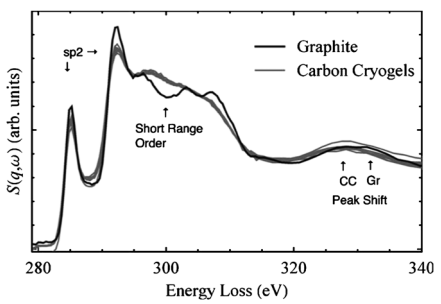

Fig. 1 XRS of various pyrolyzed and activated CCs compared to graphite.[68]

to potentially allowing the formation of nitrogen compounds (like imines) to take place in the polycondensation.[37,76,77]

In pure *tert*-butanol, the hexamine acts as a reactive catalyst to produce a nanostructure that combines fine micropores (<2 nm) with the added benefit of high macropore volumes and porosity exceeding 70%. This reduces the syneresis and subsequent shrinkage of the gels during drying, a feature uncommon in metal ion catalyzed gels. Fourier transform infrared spectroscopy (FTIR) spectra suggest new molecules or bonds that are different from those found in the metal ion catalyzed gels using the same precursor monomers. A peak at 1665 cm^{-1} suggests the presence of an imine or imino, a possible product of hexamine's protonation.

With the addition of water to the solvent, hexamine decomposes into formaldehyde and ammonia. This produces a pore structure that resembles a based catalyzed system and the macropore volume is significantly reduced to approximately 20% porosity. Moreover, the mesopore size is reduced to less than 7 nm. Typical TEM images are shown in Fig. 3, illustrating the different structures obtained for various catalysts and solvent mixtures.

For the sake of comparison with a hexamine catalyzed resorcinol-furaldehyde gel, a CC catalyzed with NaOH and a commercial sample prepared from coconut shells (referred to as YP17) were used. According to X-ray photoelectron spectroscopy (XPS), the dominant impurity in the hexamine catalyzed sample was oxygen at 1.8 atomic %. On the other hand, YP17 and the NaOH catalyzed samples had much higher concentrations of oxygen, 7.8 and 16.7% respectively. The NaOH sample also contained 2.0% Na and 4.2% Si, whereas the HTMA and YP17 samples showed no evidence of these elements. Furthermore, nitrogen adsorption isotherms indicate that YP17 has the largest surface area at 1334 $m^2\ g^{-1}$ and micropore diameter of 1.58 nm. The HTMA catalyzed sample has the next highest surface area (1063 $m^2\ g^{-1}$) but the lowest micropore diameter (1.48 nm). The sample catalyzed by NaOH has the lowest surface area at 589 $m^2\ g^{-1}$ and a micropore diameter of 1.52 nm.

Porous resorcinol-formaldehyde carbon cryogels were subjected to surface chemistry modification with nitrogen and boron after gelation, but prior to freeze drying, through solvent exchange.[78,79] During the first solvent exchange step, 2 wt% of ammonia borane (AB) was dissolved in *tert*-butanol. The rest of the solvent exchange process was done using fresh *tert*-butanol to avoid precipitation of residual AB in the pores of the gels. The SEM images of RF (organic resorcinol-formaldehyde gel) and CC (carbon cryogel) samples are shown in Fig. 4. The modified

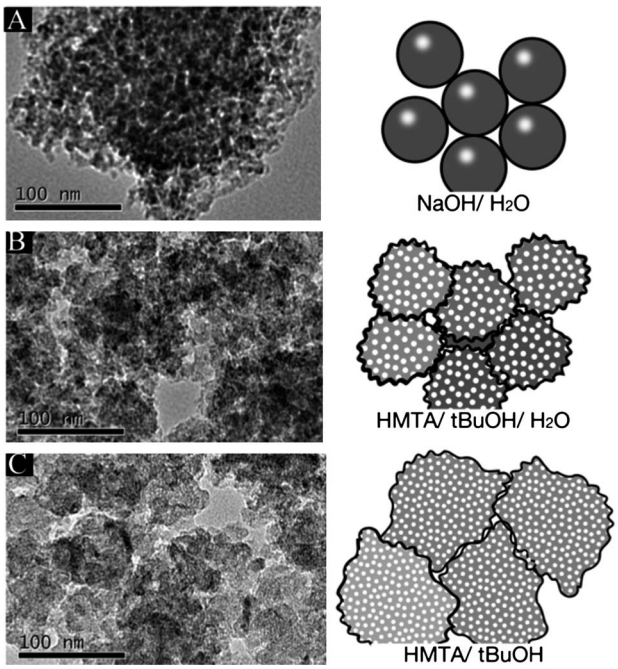

Fig. 3 Left, TEM images of pyrolyzed RF cryogels prepared with (a) NaOH catalyst in water, (b) HTMA catalyst in a solvent mixture of *tert*-butanol and water, and (c) HTMA catalyst in *tert*-butanol only. Right, schematic representation of the particles produced by different syntheses. High concentrations of HTMA promote a larger, more deformed structure.[65]

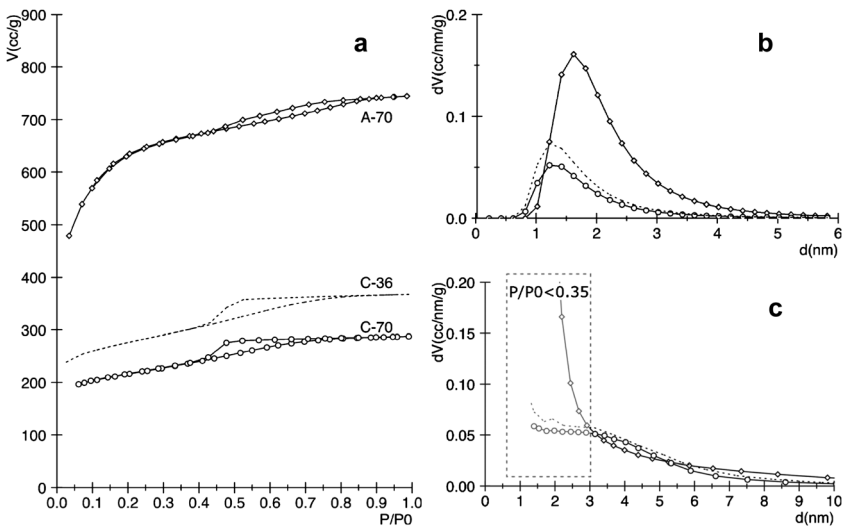

Fig. 2 (a) Isotherms of samples with various compositions and activations. (b) DA distribution and (c) BJH distribution from adsorption isotherms.[68]

cryogel samples (BNRF), shown in Fig. 3b, has a similar morphology to the RF samples (Fig. 4a). However, after pyrolysis, the morphology of CC and BNCC is very different (Fig. 4c–f). A more ordered porous structure consisting of smaller particles is observed in the modified sample (Fig. 4c and f). Although the exact mechanism causing such an appreciable difference is not known, the coating of B and N on the inner surface of RF would result in the coating of the inner surface of the carbon network upon pyrolysis as a result of the decomposition of ammonia borane. The presence of nitrogen and/or boron chemically bonded to the carbon network may hinder or prevent the coarsening of the network through sintering. Consequently, higher pore volume with smaller uniform pores would be retained. XPS measurements on the cross-section of the CC samples reveal the elemental changes in the modified sample due to the incorporation of AB throughout the carbon structure. Strong C1s, O1s, and B1s peaks were observed in the modified sample, in addition to a very weak N1s peak (about 0.1 at%). A different surface chemistry is also observed for the BNCC sample, where 2.2 wt% (2.5 at%) boron is seen and the oxygen content tripled compared to the CC sample. Also noticed is the reduction in sodium levels in the BNCC sample, decreasing from 0.6 to 0 wt%. The low N to B ratio and the high O content in BNCC may suggest that N leaves the pyrolyzed samples and B is retained, first as B-t-butoxide and then as B–OH after pyrolysis.

The pore size distributions of the RF and BNRF samples show similar distributions, with pore radii *ca.* 5 nm, and the RF sample having a wider distribution (Fig. 5a). After pyrolysis, the pores in the CC sample shift from a 5 nm radius to 16 nm and have a broad distribution of sizes. Conversely, the BNCC sample has a more uniform pore size distribution and a dominant concentration of pores of radius 6 nm appears (Fig. 5b). These structural changes suggest that the boron–nitrogen co-doping alters the surface chemistry and prevents changes, at least in the mesopore region. The mesopore volume of the CC sample slightly increases after pyrolysis, while that of BNCC significantly increases, indicating that the porous network in the BNCC is enhanced by pyrolysis. Also the surface areas of the samples CC and BNCC are quite similar.

To introduce nitrogen to a carbon network, nitrogen-rich monomers, such as melamine, have been used as precursors to increase the surface functionality.[80,81] Different methods that can be used to introduce nitrogen-containing molecules onto the pore surface of porous carbon included chemical modification through solvent exchange, the addition of conductive polymers such as polyaniline and polypyrrol,[82–85] or sublimation of nitrogen-containing molecules.[86] Hexamine was used in our research by sublimating into carbon cryogels after activation. This molecule, which is already used as a reactive catalyst in the production of CCs, decomposes through pyrolysis into heterocyclic and aliphatic structures rich in nitrogen and (iso)cyanic compounds.[87] One advantage of utilizing hexamine is the absence of oxygen as part of its molecular structure, preventing the introduction of oxygen impurities to the carbon network, which can be detrimental in some applications.

Fig. 6 shows the XPS results from both porous carbon (CC) and nitrogen-modified porous carbon (NCC). The composition of nitrogen in NCC was *ca.* 14%, a higher percentage than that obtained by previous studies using ammonia gas or other methods to introduce nitrogen compounds.[88,81,89,86] The oxygen content was *ca.* 3 at%, which is close to the 2% concentration of oxygen found in the pure carbon cryogels. The nitrogen signal in the NCC sample had a bimodal distribution. One peak was located at the binding energy of 399 eV (usually ascribed to nitrogen in heterocyclic structures) and a second peak group was located at 397–396 eV (ascribed to (iso)cyanic groups). The (iso)cyanide compounds formed in the NCC sample were likely from the carbon's adsorption of these species during the pyrolysis process, as carbon's porous structure is highly energetic and can adsorb a variety of molecules.[1] The (iso)cyanide groups are of the form $R-{}^{+}N{\equiv}C^{-}$ and usually break away from the R group during pyrolysis of the material. For this reason, peaks at this level were not found in many of the literature results that use high pyrolysis temperatures for nitrogen-rich materials.[86]

The nitrogen sorption isotherms of the CC and NCC samples looked very similar, with most of the pores in the *meso-* and macropore regions and wide size distributions, as shown in Fig. 7. However, in the NCC sample the desorption isotherm

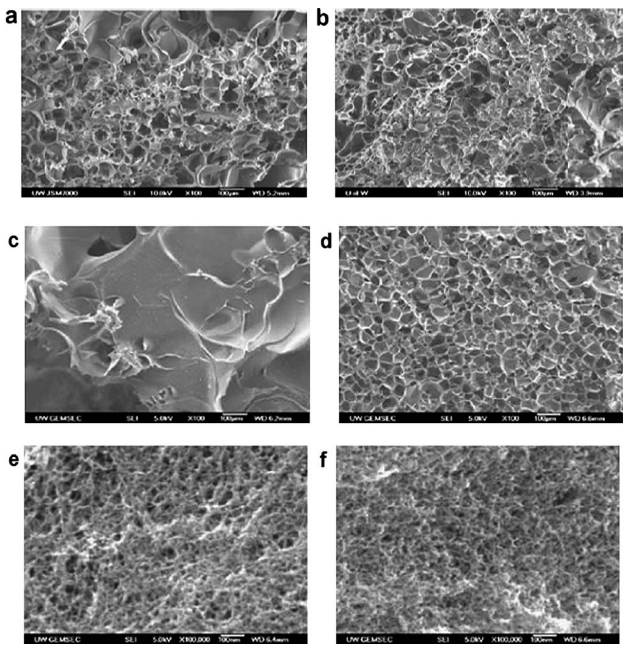

Fig. 4 SEM images of (a) RF and (b) BNRF samples (scale bar = 100 μm), (c) CC and (d) BNCC (scale bar = 100 μm), and (e) CC and (f) BNCC samples (scale bar = 100 nm).[79]

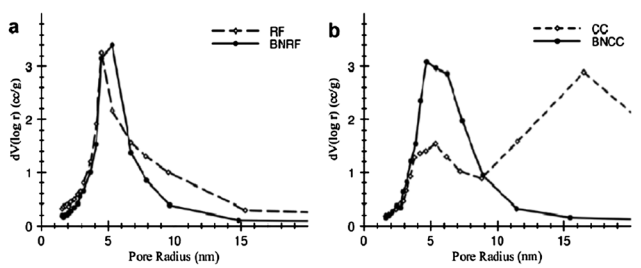

Fig. 5 BJH pore size distribution of (a) RF, BNRF and (b) CC, BNCC samples.[79]

diverged at low relative pressures, an indication of a structural change or a chemical alteration in the mesopore and micropore regions.[71] On the other hand, the similarities of both curves suggest that the structure of the porous carbon is still present. The fact that the structure is preserved makes the hexamine sublimation process described herein suitable for other types of porous carbon structures, such as ordered mesoporous carbons.[89–91]

Fig. 7b and c compare the pore size distribution of the porous carbon and nitrogen-modified carbon samples. They showed a marked decrease of the micropore volume, caused by micropores filling with nitrogen groups, while little change in the mesopore volume is observed. The micropore size increases slightly from 1.2 to 1.68 nm, another indication that the micropores might be filled, leaving only the larger pores accessible to N_2 adsorption. The disappearance of the micropore volume in the NCC sample by the entrapment of nitrogen compounds can be explained by the increased surface energy produced by the high curvature of the micropores.[71] The surface area of the samples supports this finding since the NCC sample had similar mesopore and macropore areas as compared to the CC sample, while no micropore area was detected.

3. Highly porous carbon for supercapacitors

The most efficient hybrid vehicles lack power and the models that accelerate quickly do so with the assistance of large internal combustion engines. This significantly degrades their fuel efficiency – barely making the extra cost worthwhile in terms of fuel efficiency.[92] While the batteries in these vehicles are capable of storing large quantities of energy, they cannot be charged or discharged quickly. This lack of power density requires the battery packs to be oversized, resulting in increased vehicle weight and reduced efficiency. As with the poor discharge rate, battery charging is limited by the same kinetics, thus reducing efficiency gains through full regenerative braking. Additionally, the peak power demands that are placed on the battery packs degrade the life of the battery, reducing the overall longevity of the vehicle.[93] An ideal electrical energy storage device will have high cycle life as well as high energy and power density when measured in terms of weight, volume, and cost.

Supercapacitors, also known as Electric Double Layer Capacitors (EDLCs), operate by adsorbing/desorbing charged ions from an electrolyte onto their highly porous high surface area electrodes. While traditional capacitors rely on a dielectric material to store a charge, EDLCs rely on the charge of the

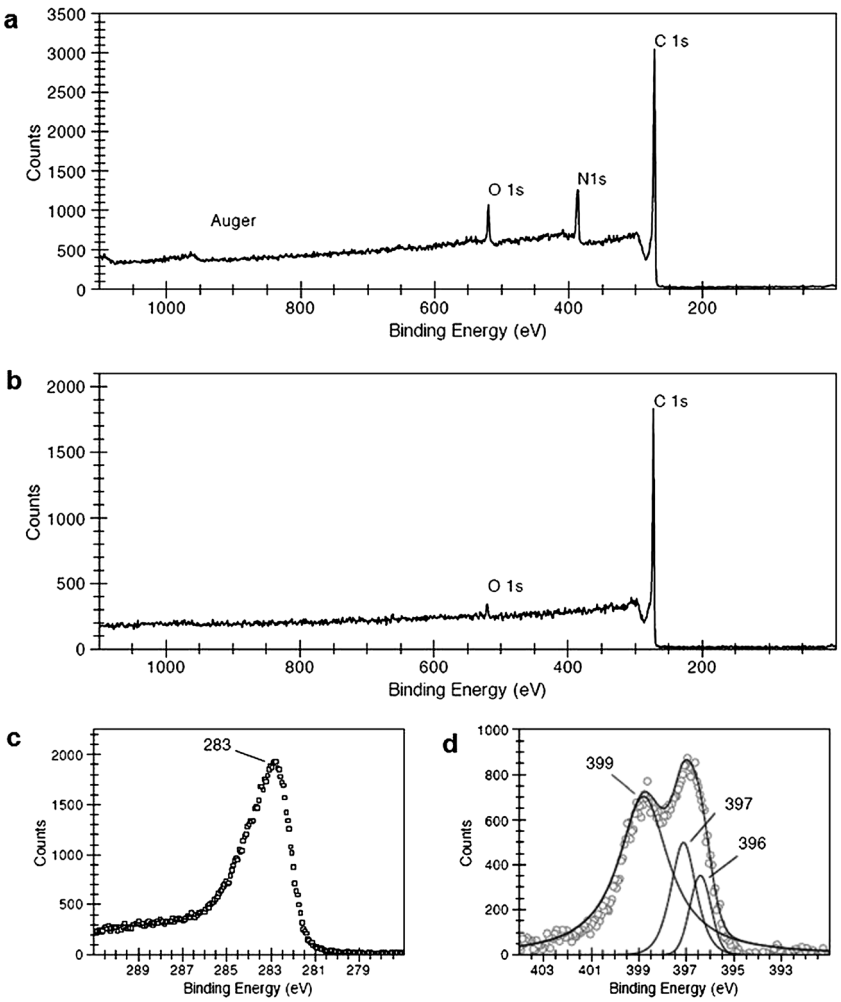

Fig. 6 XPS data for (a) NCC and (b) CC, and corrected positions of the 1s peaks for (c) carbon and (d) nitrogen.[74]

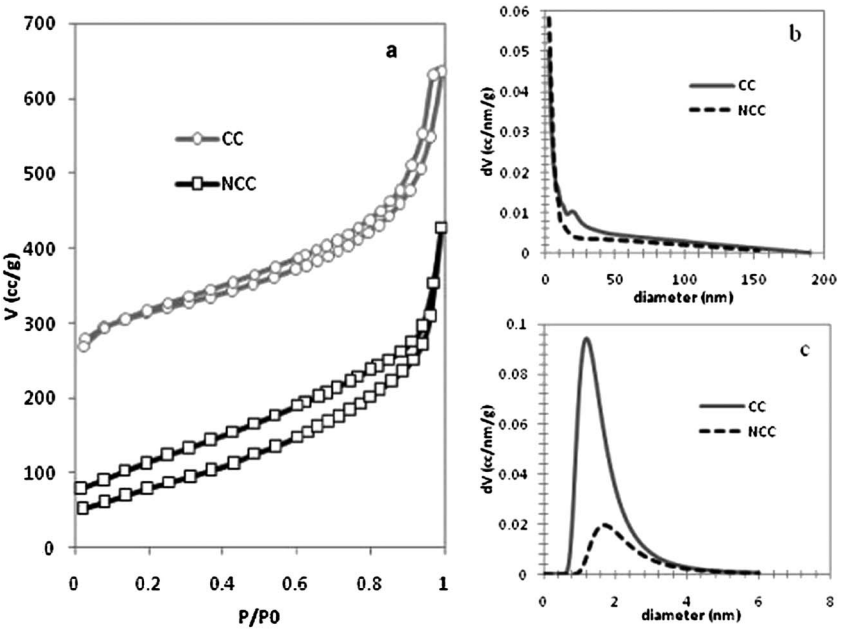

Fig. 7 (a) Nitrogen sorption isotherms at 77 K of the CC and NCC samples. Both isotherms have similar shapes at $P/P_0 > 0.3$, indicating similar mesoporous structure. Micropores experienced the most drastic change in volume. (b) BJH pore size distribution, showing only a small difference between the mesopores in the CC sample and the NCC sample. (c) DA micropore size distribution, showing the increase in pore size and decrease in micropore volume when comparing CC to NCC.

adsorbed double layer. The capacitance of traditional dielectric capacitors is limited by the thickness of the dielectric material, which separates the charge. The thinnest dielectric materials are 2–5μm in thickness.[94] However, in the case of EDLCs, charging is achieved by dissociation of ions in the electrolyte salts, resulting in charge separation distances on the order of 1nm. This arrangement occurs inside the pores of high surface area carbon materials.

Current EDLCs in the market are produced by pyrolyzing and activating wood, plant matter, petroleum sources, and phenolic resins (including aerogels and cryogels), among others.[95,96] Naturally derived electrodes contain great amounts of impurities or ash content, which can compromise the EDLC performance[97] due to unwanted *Faradaic* reactions that can degrade the electrolyte. In addition, the pore size is limited by what nature provides and may vary from source to source. Carbon nanotubes have also been used in the manufacturing of batteries and supercapacitors, mainly because of their high conductivity. Unfortunately, their high cost and mesoporous structure only allow low charge storage compared to nanoporous activated carbons (180 F/g *vs. ca.* 300 F/g in aqueous electrolytes).[96,98] Sol–gel derived carbon cryogels and carbon aerogels, on the other hand, have good conductivity, high surface area, controlled bulk and surface chemistry, and tunable porous structure, rendering them excellent candidates as electrodes for supercapacitors with high energy density and long cyclic stability.[99–102] Our research has been mainly focused on the understanding the relationship between electrical energy storage performance and porous structure and chemistry of porous carbon, rather than the seeking high storage capacity. Electrochemical impedance spectroscopy (EIS), along with other characterization techniques, has been intensively used in the study of carbon cryogels with surface and bulk chemical modification. All samples are tested in two-electrode configurations with tetraethylammonium tetrafluoroborate (TEATFB) in saturated 50/50 propylene carbonate/dimethylcarbonate as the electrolyte. Cyclic voltammetry (CV) is performed at scan rates of 100, 50, and 10 mV s^{-1} while galvanic cycles (GC) are measured at 100, 50, 10, 5,1, and 0.5 mA using a voltage range between 0 and 2 V. For EIS, samples were pretreated at +2 V and cycled with an AC voltage amplitude of 10 mV and a frequency range of 0.1 MHz–1 mHz.[74,79]

Carbon cryogels doped with both nitrogen and boron demonstrated different CV curves; two distinct current peaks were observed during the first two cycles at a scan rate of 100 mV s^{-1} (Fig. 8a), but were absent in a similar measurement for the CC sample (Fig. 8b). Incorporation of nitrogen or other dopants in carbon structures has been shown to create pseudocapacitive effects, as reported in literature.[103,104]

Fig. 9 shows the progression for three applied currents during galvanic cycling (GC). At applied currents of 5 mA and higher, the GC curve of the B and N co-doped carbon cryogel sample is symmetric, similar to that of the CC sample. As the current decreases below 1 mA, *Faradaic* reactions render the GC curve asymmetric, and ultimately at 0.5 mA prevent the capacitor from charging to the intended potential. This asymmetry is evidently due to possible redox reactions involved with the functional groups from the surface modification of the carbon matrix. Although the exact electrical conductivity of carbon cryogel is not known, it is reasonable to assume it has a similar conductivity to that of carbon aerogel, which is on the order of 1 S cm^{-1}.[99] The incorporation of nitrogen and/or boron onto the surface of the carbon network would have relatively small impact on the electrical conductivity of the carbon network itself. However, the surface nitrogen and boron are expected to exert noticeable impact on the charge transfer cross the interface.

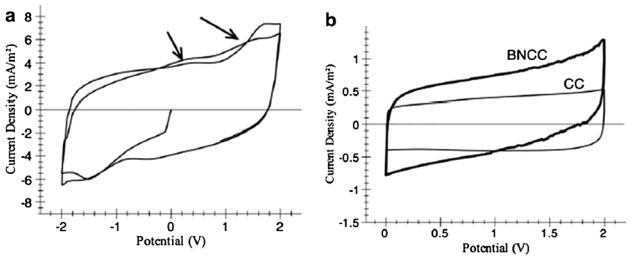

Fig. 8 (a) First cyclic voltammograms at a rate of 100 mV s^{-1} for BNCC, arrows point to *Faradaic* reactions. (b) Cyclic voltammograms of BNCC and CC samples.[79]

Fig. 10 compares the capacitances per unit specific surface area as a function of reciprocal square-root of voltage rate, $1/\sqrt{v}$, for the BNCC and CC samples. The carbon co-doped with B and N possessed 30% higher specific capacitance than that of the CC at higher frequencies. Such increase in the specific capacitance are *Faradaic* in nature, either from dopants or B_2O_3. This improved capacitive behavior has been observed in carbon materials due to the presence of active species, which contribute to the total specific capacitance by the pseudocapacitive effect. At the same time, large specific surface area and porosity are also essential for high current density and charge storage.[68,105,104,97]

However, at the low frequency range, the CC electrodes show signs of pore exhaustion and ideal capacitor behavior,[68] while the BNCC samples deviate from ideality, also seen in the lower phase angle at $f = 0.01$ (Fig. 11b and c). This deviation is likely due to *Faradaic* reactions in the BNCC electrodes. These results strongly suggested that the dopant in the BNCC samples is electrochemically active and has introduced other charged species during potential cycling, while the CC sample relies

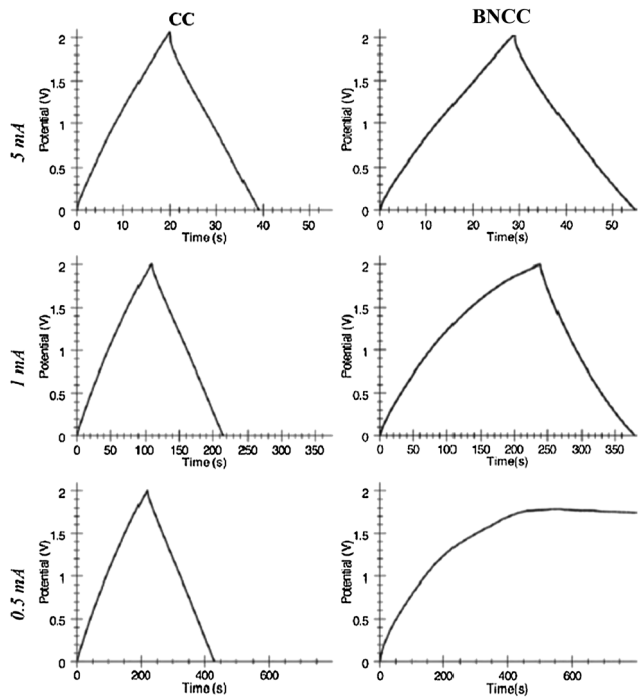

Fig. 9 Galvanic cycles of CC and BNCC at 5, 1, and 0.5 mA. Notice the BNCC surface modification is chemically active as seen at low currents. The CC sample, on the other hand, does not exhibit this behavior.[79]

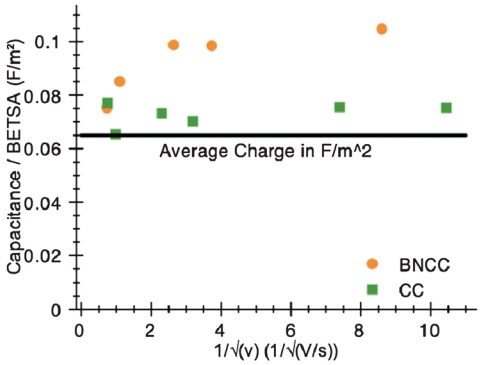

Fig. 10 Capacitance of samples *vs.* $1/\sqrt{v}$. The constant behavior of CC is characteristic of mesopores or larger pore structures that are not affected by the electrolyte penetration.[106] On the other hand, pseudocapacitance increases the charge storage capabilities of carbon in the BNCC sample.[79]

completely on the electrolyte for active species in forming the electric double-layers.

Faradaic reactions also affected the charge/discharge rate when impurities were present in the capacitor.[107,108] In Fig. 12a, the galvanic cycles at 1 mA for the HMTA electrodes were almost perfectly linear, expected of an electric double layer capacitor. This linear behavior remained even after 10,000 cycles. In Fig. 12b and c, the *Faradaic* reactions were evident from the non-linear charge and discharge cycles. Initially, YP17 had an asymmetric charge/discharge. The linear discharge of YP17 can be attributed to a charge selective *Faradaic* reaction, in this case from the oxygen-containing functional groups in the carbon. The *Faradaic* component in YP17 decreased after 10 K cycles, behaving like an EDL capacitor, which is indicated by the charge and discharge curves becoming symmetric. In Fig. 12c, the NaOH catalyzed sample shows both charge and discharge cycles characteristic of *Faradaic* reactions, which diminished after 10 K cycles. However, unlike the YP17 sample, both the charge and discharge curves retain the same voltage rate, seen in reversible processes. This is likely due to the Na+ and OH− ions from the NaOH catalyst left in the carbon.

The impedance spectra of the supercapacitors show how the pure carbon HMTA sample compares to the commercial sample YP17. The NaOH sample was not included since little variation was observed from this plot. At the high frequency range of the spectra, the HMTA sample had a large equivalent series resistance (ESR) prior to the repetitive cycling. This resistance was over 6 times greater than that of the YP17 sample. However after 10 K cycles, the resistances of both samples YP17 and HMTA are almost indistinguishable. The reduction of the ESR in HMTA was enhanced by increased penetration of the electrolyte ions within the porous network. However, YP17 increased its ESR, which can be attributed to the consumption of the oxygen *Faradaic* contribution that originally decreased its ESR. The *Faradaic* reaction developed in the low frequency impedance spectra, as shown in Fig. 13b. While the HMTA sample has a linear, almost perpendicular spectrum characteristic of electric double layer supercapacitors before and after cycling (squares in Fig. 13b), the YP17 sample forms an arch (open circles in Fig. 13b), indicative of *Faradaic* reactions. After repeated cycling, this *Faradaic* component disappears (closed circles in Fig. 13b).

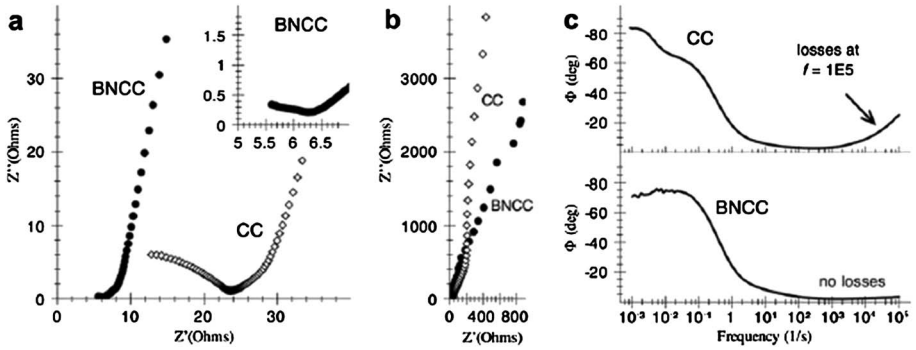

Fig. 11 (a) Nyquist plot at high frequency (bulk impedance), (b) low frequency, and (c) phase angle/losses.[79]

These results demonstrate that the capacitance per surface area can be increased by 18% over that of the commercial sample (*ca.* 0.08 F/m^2) without the use of *Faradaic* reactions. However, as seen previously by doping CCs with ammonia borane, *Faradaic* reactions can be used to increase the capacitance. Nitrogen functional groups and nitrogen doping are already considered as ways to increase the conductivity of carbon, even when it is electrically insulating (like amorphous sp^3 carbon).[2] Some mechanisms that are known to enhance the conductivity and charge storage capacity of carbon include bond structure, active redox sites, and delocalization of charge (ions or electrons).[109,88,110] In supercapacitors that use aqueous electrolytes, the capacitance can increase to up to 3 times higher than that of electric double-layer supercapacitors by promoting redox reactions.[109,88,110] While redox reactions are responsible for the pseudocapacitance in aqueous electrolytes, in organic electrolytes, another mechanism is present. Few studies have tested the performance of nitrogen-doped carbon in organic electrolytes.[81]

Though the exact mechanism is unknown, one proposed explanation is *Faradaic* reactions[111] induced by lone electron pairs from the nitrogen groups interacting with the cations in the electrolyte. The following are possible reactions that could be taking place on the nitrogen-modified carbon surface:

$$\text{–C–NH}_2\text{: } + (C_2H_5)_4^+ \leftrightarrow \text{–C–NH}_2\text{: } (C_2H_5)_4^+ \quad (1)$$

$$\text{–C=NH: } + (C_2H_5)_4^+ \leftrightarrow \text{–C=NH: } (C_2H_5)_4^+ \quad (2)$$

$$\text{–C}\equiv\text{N: } + (C_2H_5)_4^+ \leftrightarrow \text{–C}\equiv\text{N: } (C_2H_5)_4^+ \quad (3)$$

As is typical with unmodified carbon, there is a loss in capacitance for the CC electrode after cycling. After 1,000 cycles, the capacitance of the CC device drops by approximately 22%. However, the NCC device experiences only a modest loss in capacitance after 1,000 cycles, dropping by just 5%. The differences in cycling behavior between the two samples are even more dramatic when the devices are cycled 10,000 times. This can be seen in Fig. 14, where the CC device experiences increased discharge slopes at both high current densities (5 mA cm^{-2}, Fig. 14a) and low current densities (0.5 mA cm^{-2}, Fig. 14b). The NCC electrode, on the other hand, retained its current density, and hence its charge, as the supercapacitor was cycled extensively. One scenario that can explain this is that the nitrogen is helping to reduce the aging of the electrolyte.[112] However, the galvanic cycles suggest that the nitrogen functional groups were being activated with capacitor cycling. The resulting effect can be seen in Fig. 14c and d. After cycling the electrode 10,000 times at a high current density of 5 mA cm^{-2}, the capacitor experienced only a modest loss in the capacitance, expressed in Fig. 14c as an increased discharge slope. However, the active material is still within the small micropores and at a low current density of 0.5 mA cm^{-2}, the capacitance increased (a reduction in the discharge slope, shown in Fig. 14d) after 10,000 cycles, *i.e.* more charge was generated as the device was cycled. This mechanism can provide a way to compensate for the loss of capacitance seen in the purer carbon electrodes. Notice that the pseudocapacitance effect can be seen when the NCC electrode is measured using a three electrode test cell (Fig. 14e and f). This effect was not noticeable in the two electrode setup.

4. Porous carbon–vanadium pentoxide nanocomposites for lithium-ion batteries

Lithium-ion batteries have replaced a great deal of older battery systems, such as nickel metal hydride, particularly in high-tech

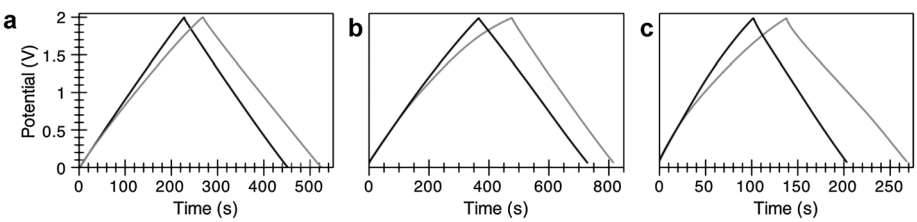

Fig. 12 Series of galvanic cycles measured at 1mA for (a) HMTA carbon, (b) coconut-based sample YP17, and (c) carbon cryogel made with NaOH. The HMTA carbon in (a) has the characteristic straight slope of a double layer capacitor in both the charge and discharge cycles. (b) and (c) show non-linear behavior characteristic of *Faradaic* reactions. The gray curve is the initial cycle and the black curve is after 10 K cycles.[74]

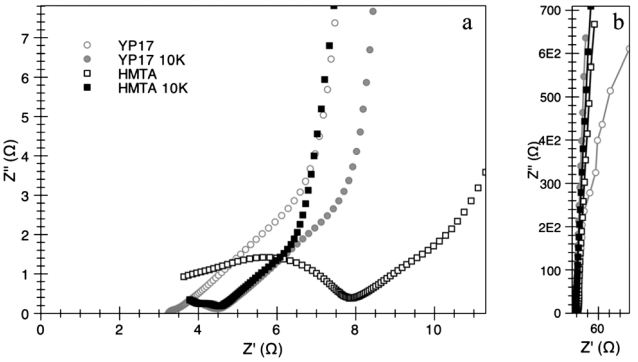

Fig. 13 (a) ESR and (b) low frequency impedance data. The *Faradaic* reactions from YP17 can be seen in the sample prior to cycling in the low frequency data. After cycling, the capacitor behaves more like a double layer capacitor. The HMTA sample does not have this *Faradaic* effect and the resistance is greatly reduced after cycling.[79]

devices like laptops and cell phones. This is primarily due to their high energy density and long cycle life.[113–115] However, lithium-ion batteries still do not meet the needs for high specific power and energy storage applications, such as power tools, electric vehicles, and efficient use of renewable energies.[116] Developing new cathode and anode materials with better energy storage properties has become an urgent demand to meet the increasingly

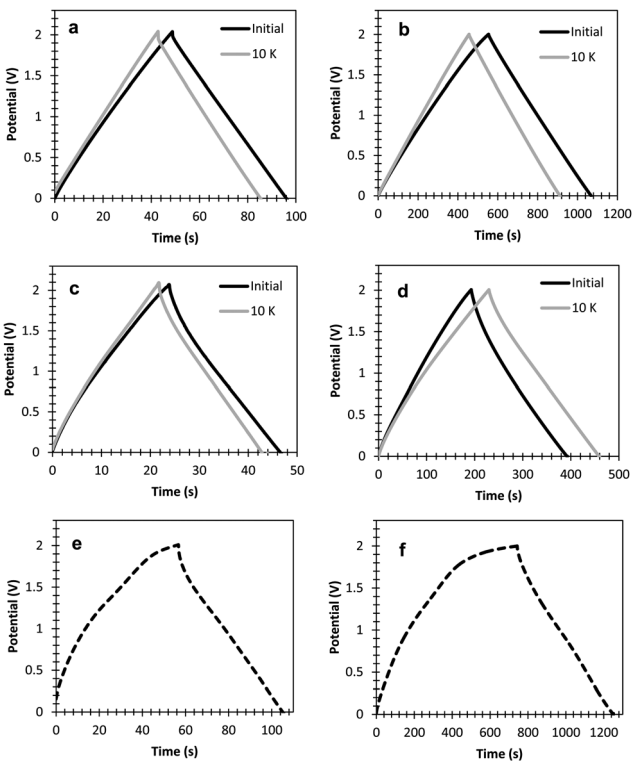

Fig. 14 Galvanic cycles for CC cycled at (a) 5 mA cm^{-2} and (b) 0.5 mA cm^{-2}, and NCC showing (c) a loss of capacitance during discharge at 5 mA cm^{-2}, and (d) gain of capacitance at 0.5 mA cm^{-2}. The black line is the initial cycle and the gray line is after 10,000 cycles. (e) and (f) represent initial galvanic cycles of the 3-electrode test cell at 5 mA cm^{-2} and 0.5 mA cm^{-2}, respectively.

strict requirements of new technologies and industries. Vanadium pentoxide (V_2O_5) has been one of the attractive candidates for cathode materials, due to its high energy density, intercalation voltage (*versus* the anode material), reversibility, and stability.[117–119] However, the intrinsic low diffusion coefficient of lithium ions in crystalline V_2O_5 (*i.e.*, $D \sim 10^{-12}$ cm^2 s^{-1})[120] hinders the practical wide-spread utilization of this material as a cathode. The low electronic conductivity of V_2O_5 is another key factor that should be addressed for applications as an electrode material. Composites of V_2O_5 with highly electrically conductive materials, such as conductive polymers,[121,122] metal fibers,[123] and carbonaceous materials, have attracted great attention for lithium-ion batteries.

In our lab, nanoscale hydrous vanadium pentoxide was deposited throughout mesoporous carbon cryogel films using potentiodynamic electrodeposition from $VOSO_4$ solution.[124] This is similar to anodic electrodeposition,[125] but under an alternating electric field. Fig. 15 shows a schematic of the synthesis of the $V_2O_5 \cdot nH_2O$-CCs nanocomposites. This reactions occurs as follows:

$$2VO^{2+} + 3H_2O \rightarrow V_2O_5 + 6H^+ + 2e \quad (4)$$

The formation of hydrous vanadium pentoxide is indicated by the rapid increase of the oxidation current density starting from 1.1V and reaching a maximum at 1.5 V (*vs.* Ag/AgCl), as shown in Fig. 16. With the increased number of sweeping cycles, the current density of the oxidation peaks continuously became lower due to the formation of relatively insulating hydrous vanadium pentoxide coating on the surface of carbon cryogel scaffold. At potentials higher than 1.7V, a second rapid increase of current density was observed, which corresponds to the oxidation of water.

Fig. 17 shows the nitrogen sorption isotherms for both coherent $V_2O_5 \cdot nH_2O$-CCs nanocomposites and pristine carbon scaffold samples. Both exhibit typical IV isotherms,[126] with a hysteresis associated with the dominance of mesoporosity. After deposition of hydrous vanadium pentoxide, the amount of nitrogen adsorbed onto the sample decreased significantly (Fig. 17a), which suggested a decrease in pore volume in coherent nanocomposites as compared to pristine carbon cryogels. The pore size distributions of carbon cryogels and coherent carbon cryogel–hydrous vanadium pentoxide nanocomposites (Fig. 17b) show the peak pore size shifted to a smaller size after the deposition of hydrous vanadium pentoxide. After the deposition, the pore volume reduced significantly from 0.98 cc/g to 0.42 cc/g, with a reduction of more than 50%. Also, the peak pore size decreased from 8 nm to 6 nm in diameter and the surface area decreased from 572 m^2 g^{-1} to 402 m^2 g^{-1}. The reduction in the pore volume, pore size, and specific surface area were all presumably due to the successful deposition of hydrous vanadium pentoxide inside the pores of the carbon cryogel, filling some of the void space and thus resulting in the change of the porous structure.

SEM images shown in Fig. 18 and Energy-dispersive X-ray spectroscopy (EDAX) analyses (not shown) reveal a homogeneous morphology across the sample, suggesting uniform deposition of hydrous vanadium pentoxide throughout the

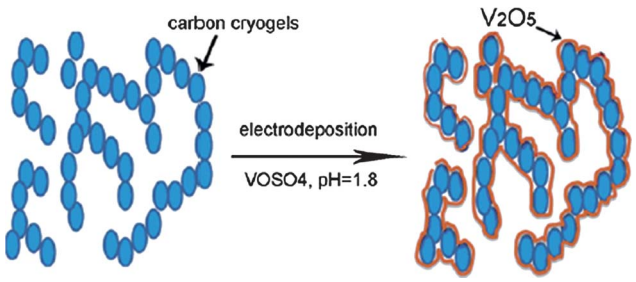

Fig. 15 Schematic illustrating the synthesis and microstructure of coherent nanocomposites in which hydrous V_2O_5 is deposited onto the surface of the carbon cryogel scaffold.[124]

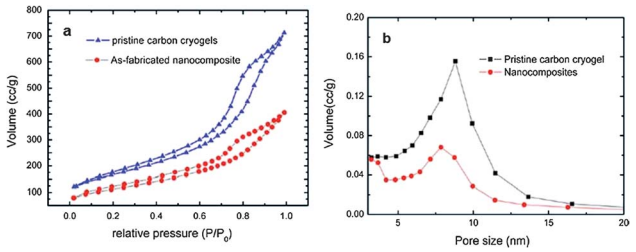

Fig. 17 (a) Nitrogen sorption isotherms and (b) pore size distributions for $V_2O_5 \cdot nH_2O$-CC nanocomposites and pristine CCs.[124]

porous carbon cryogel film, in contrast to a coated layer of oxide on the exterior surface of the carbon cryogel film. The X-ray diffraction (XRD) analyses revealed that no characteristic peaks were detected for nanocomposites before thermal annealing, which indicated the amorphous nature of the nanocomposites. When annealed at 400 °C in air for 2 h, crystallized V_2O_5 was formed, as indicated by the XRD pattern of orthorhombic V_2O_5.

Fig. 19 displays the cyclic voltammograms of the $V_2O_5 \cdot nH_2O$-CCs nanocomposite, $V_2O_5 \cdot nH_2O$ film, and pristine CC film electrodes, measured using an electrolyte consisting of 1 M $LiClO_4$ in PC at the potential scan rate of 1mV s^{-1}. The voltage window was set between −1.5 and 0.5V (*vs.*$Ag/AgNO_3$) and the current density was normalized to the mass of the samples. Two current peaks at around −0.85 and −0.6V *vs.* Ag/Ag^+ in the anodic scan and two peaks at around −1.0 and −0.7 V *vs.* Ag/Ag^+ in the cathodic scan were identified in the CV curves of the V_2O_5 thin film. It is believed that the pairs of anodic and cathodic peaks in the CV curve are related to the Li-ion intercalation and de-intercalation, respectively.[127] For the coherent hydrous vanadium pentoxide - carbon cryogel nanocomposites, peaks were broader and overlap centered near −0.7 V in the cathodic scan and −0.6V in the anodic scan. These changes may be attributed to the different electrochemical potentials caused by the new environment surrounding V_2O_5 due to the amorphous

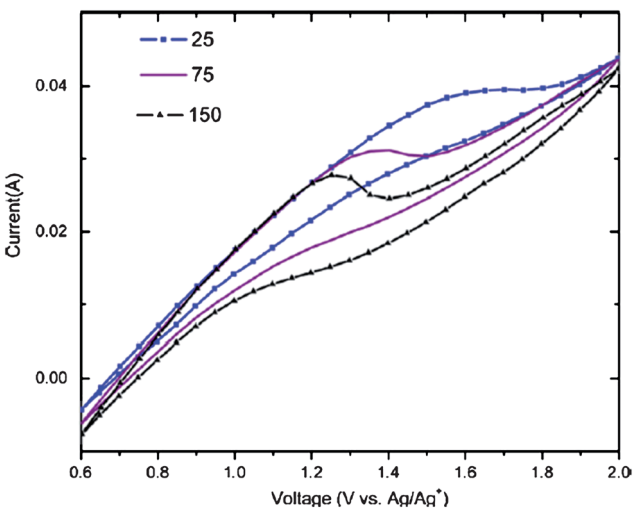

Fig. 16 Cyclic voltammetry curves for deposition on carbon cryogels in the voltage range of 0.6–2.0V *vs.* Ag/Ag^+ at a scan rate of 50 mV s^{-1}. The solution was 0.1 M $VOSO_4$ and the pH was adjusted to 1.8.[124]

carbon cryogels for lithium-ion intercalation and de-intercalation. Neither cathodic nor anodic peaks for the CC film were observed, which demonstrated that no lithium-ion electrochemical intercalation into the carbon cryogel substrate occurred within this voltage window. Thus the insertion and removal of lithium ions are attributed to hydrous vanadium pentoxide during the charge and discharge process.

The specific discharge/charge capacities of $V_2O_5 \cdot nH_2O$-CCs nanocomposites and $V_2O_5 \cdot nH_2O$ films are shown in Fig. 20. The $V_2O_5 \cdot nH_2O$ film deposited on a platinum substrate possessed an initial specific discharge capacity of 151 mAh/g at a current density of 100 mA g^{-1} and had a continuous loss in the successive cycles. A capacity of 96 mAh/g was retained after 20 cycles, which only accounted for 63.5% of the initial discharge capacity. The hydrous vanadium pentoxide in the coherent $V_2O_5 \cdot nH_2O$-CCs nanocomposite reached 280 mAh/g for the initial discharge cycle and the specific discharge capacity remained quite stable for the later cycles. The specific discharge capacity of hydrous vanadium pentoxide in the coherent nanocomposites still possessed a capacity of 257 mAh/g after twenty cycles, showing a capacity reduction of only 0.5% per cycle.

Materials with good electrical conductivity and mass transport are key factors for the success of lithium-ion batteries. The relatively low specific capacity of$V_2O_5 \cdot nH_2O$ films could be attributed to the fact that the electrochemical utilization of vanadium pentoxide was limited to the relatively thin surface layer of the oxide film.[128] In contrast, hydrous vanadium pentoxide in the nanocomposite may be responsible for all of the lithium intercalation and de-intercalation, as the introduction of the porous carbon scaffold (carbon cryogel) effectively reduced the diffusion distance for both mass and charge, and created large specific surface area for the intercalation and de-intercalation reactions. Coherent $V_2O_5.nH_2O$-CCs nanocomposites with an average pore size 6 nm could facilitate passage for lithium ions and thus, increased the active contact surface area (>400 m^2 g^{-1}) with vanadium pentoxide and resulted in much higher capacities. The nanocomposites also demonstrated much improved reversibility of the discharge and charge processes. This may be partly due to the porous structure, which offers extra space to accommodate the stresses induced by lithium ion intercaltion/de-intercalation, as well as the additional mechanical support provided by the coherent carbon network.

While the exact microstructure of the coherent nanocomposites is not known, the particles of hydrous vanadium pentoxide could be smaller than 1 nm in diameter if $V_2O_5 \cdot nH_2O$ formed a conformal coating onto the pore surface of carbon

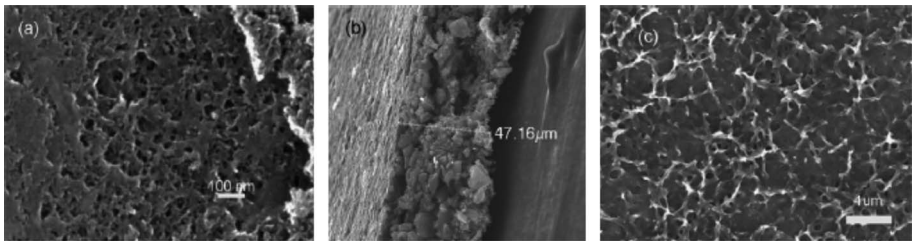

Fig. 18 SEM images of $V_2O_5 \cdot nH_2O$-CC nanocomposite (a) surface morphology, (b) cross-section, and (c) surface morphology of $V_2O_5 \cdot nH_2O$ thin film on Pt substrate.[124]

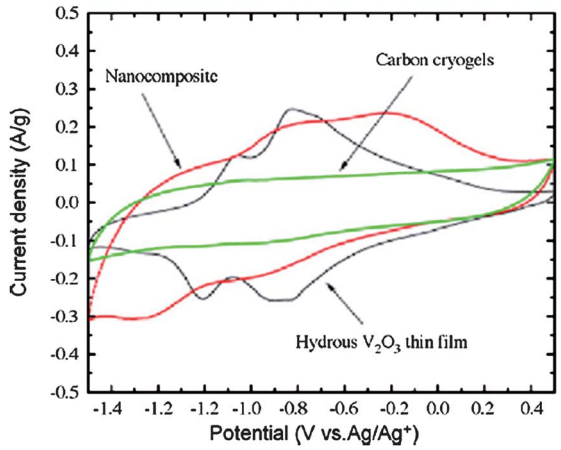

Fig. 19 Cyclic voltammetry curves of hydrous V_2O_5, CC, and $V_2O_5 \cdot nH_2O$-CC in the voltage window between 0.5 and −1.5V *vs.* Ag/Ag^+ in 1 M $LiClO_4$ in PC at the scan rate of 1 mV s^{-1}.[124]

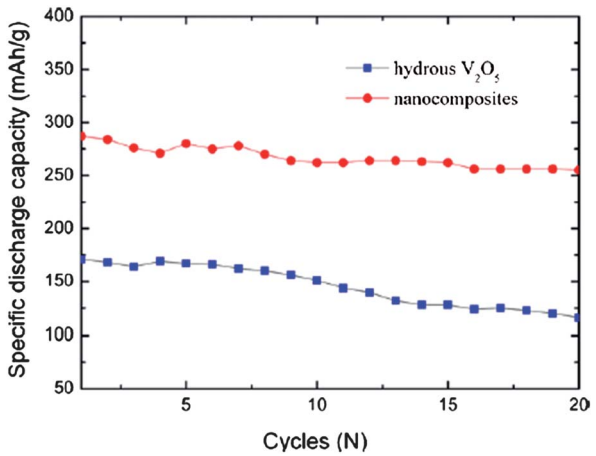

Fig. 20 Specific discharge capacity as a function of cycle number for $V_2O_5 \cdot nH_2O$-CC and $V_2O_5 \cdot nH_2O$ on Pt foil with all mass based on hydrous vanadium pentoxide.[124]

cryogels, as the pore diameter was reduced from 8 nm to 6 nm. The absence of XRD peaks before annealing in the as-grown coherent nanocomposite might be another indication of either very small particles or possible amorphous structure. Small particles with much higher surface area (>400 m^2 g^{-1}) would be beneficial to the surface or interface redox reactions during lithium-ion intercalation and de-intercalation. The large surface energy and poor crystallinity (or amorphous structure) may allow easy phase transition, leading to a greatly expanded range of reversible lithium-ion intercalation and de-intercalation. Electroactive materials with controlled nanostructures, surface defects, and poor crystallinity, for both anode and cathode applications, have been reported to achieve largely enhanced lithium-ion intercalation properties.[129–131] These properties have been attributed to the extra surface energy or non-equilibrium state of the electroactive materials. A similar explanation might be applicable to these nanocomposites.

5. Highly porous carbon for methane gas storage

Natural gas is already in relatively widespread use as a transportation fuel. According to the Natural Gas Vehicle Coalition, there are currently 112,000 Natural Gas Vehicles (NGVs) on the road in the United States today, and more than 13 million NGVs worldwide.[132] For example, Pacific Gas & Electric has 13,000 vehicles using the technology.[133] Over 30 different manufacturers produce 100 models of light, medium, and heavy-duty natural gas vehicles and engines. Roughly 26% of all new transit bus orders are for natural gas. One of the benefits of natural gas is that it produces significantly less pollution than gasoline. A natural gas powered vehicle produces 70% less carbon monoxide, 87% less NO_x, and 20% less CO_2 as compared to gasoline powered vehicles.[132] Despite a significant demand for natural gas storage onboard vehicles, the basic approach has not changed much over thirty years. The conventional approaches available today, compressed natural gas (CNG) and liquid natural gas (LNG) have significant drawbacks, including:

- Relatively high cost: The high pressures of CNG storage and the low temperatures of LNG require expensive, bulky storage systems.
- Low storage efficiency: The high compression required for CNG, and the low temperatures necessary for LNG, require significant energy, greatly reducing overall storage system efficiency.
- Safety concerns: Highly compressed gas of any kind presents a significant safety concern, especially in an on-site distributed storage model.

Compressed Natural Gas – CNG is by far the most ubiquitous type of small-scale natural gas storage; however, CNG at 250 bars has only 25% of the energy density of diesel fuel.[134] Even at this pressure, CNG requires more than twice the storage volume of LNG. These pressure vessels are also expensive and create significant safety issues. The cost of compressing the gas to 250 bars further reduces overall storage system efficiency.

Liquefied Natural Gas – LNG provides a much higher energy density than CNG, about 60% of diesel fuel, but is even more expensive to produce and store. LNG requires expensive cooling processes, sophisticated storage vessels, and suffers a continuous gas loss from boil-off. The production process consumes an energy equivalent to about one-sixth of the volume of the produced LNG. Stored in special insulated cryogenic containers, LNG uses constant boil-off to keep the remaining LNG at liquid temperatures. The high expense of producing and storing LNG makes its application impractical for small scale on-site storage.

The favored alternative to these two storage methods is natural gas adsorbed on a microporous medium such as activated carbon. The DOE has specified an adsorbed natural gas (ANG) target of $180V_g/V_v$ or 180 volumes of standard temperature and pressure NG (V_g) stored per volume of storage vessel (V_v) at a storage pressure of only 34.5 bar, as opposed to 151 bar for CNG. The gravimetric performance of a material also can be reported on a gravimetric basis as moles of methane/gram of carbon, or mol g^{-1}. Adsorbed natural gas has demonstrated storage performance competitive with CNG but at pressures that can meet the DOE target. This relatively low pressure would allow for easier tank filling, provide room for non-cylinder form factors, allow for optional tank materials, and increase the safety of a tank. In order for natural gas to become a mainstream automotive fuel, these types of storage advancements are critical.

Natural gas contains portions of ethane, propane, and butane, but the main component is methane. As such, research has focused on finding a porous material that can store adsorbed methane. Theoretical studies have shown that an optimal material engineered to enhance capillary condensation and gas adsorption would possess pores 1.5–2.5nm in diameter and a pore volume in this range of greater than 1 cc/g.[135] Activated carbon is the dominant material in this field because of its ease of processing and controllable pore structure. Other types of porous materials could be used, such as metal organic framework (MOF) materials. These also contain tunable micropores (defined by IUPAC as pores <2nm in diameter), but most work has been focused on activated carbons.[136] The bulk of the literature focuses on pyrolysis (or carbonization) and activation treatments on existing organic materials such as pitch, coconut fibers,[137] pistachio nut shells,[138–141] carbon fibers,[142] and even tire rubber.[143]

Fig. 21 shows the typical methane adsorption curves of a resorcinol-formaldehyde carbon cryogel at room temperature,[144] with volumetric and gravimetric storage as a function of pressure measured using a Sievert's apparatus.[145] Volumetric storage capacity is not a material property as it largely depends on sample compaction, but the gravimetric storage capacity is indicative of the microporous structure of the sample in question. The methane sorption curves in these carbon cryogels are similar to that of activated carbon widely reported in literature.[146,137,142]

Fig. 22 shows that the gravimetric storage capacity varies as a function of R/C (precursor resorcinol to catalyst sodium carbonate) ratio. For example, increasing the R/C value from 10 to 25 resulted in a drastic increase in methane storage capacity (~4 times), which reaches its maximum of 13 mmol g^{-1} at R/C = 50, and then decreases significantly as the R/C ratio increases further to 75. Total pore volume and surface area are also plotted in Fig. 22, showing a close correlation between all three metrics.

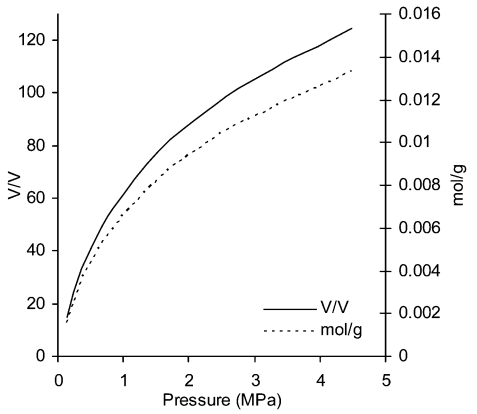

Fig. 21 Methane adsorption curves in terms of v/v and mol g^{-1} for a carbon cryogel at room temperature.

This can be easily understood when considering the fact that methane storage in carbon cryogels occurs in two mechanisms: surface adsorption (both monolayer and multilayer adsorption) and capillary condensation in micropores.

An R/C value either too high or too low is not beneficial for the storage performance of the material. Pekala[147] has shown by small angle X-ray scattering (SAXS) analysis that in the RF system, the length scale of the solid and solvent phases in the gelling RF polymer network are equal and dependant on R/C. At low R/C ratios, the width of both the pores and solid phases are very small whereas high R/C ratio results in an open structure with large pores and correspondingly large solid portions. Hence, a high R/C carbon cryogel exhibits poor methane storage capacity because the material consists of large solid chords of carbon separated by pores of an equal size, larger than that which is beneficial. Poor performance in low R/C cryogels may be explained by drying or pyrolysis induced collapse of the very small pores that result from the highest catalyst concentrations. Related behavior such as reduced micropore volume and surface area at high or low R/C ratio has been noted in the literature.[148]

Fig. 23a relates R/W (resorcinol to water ratio) to nominal powder density and storage performance. Increasing the powder density increases the amount of storage material per unit volume,

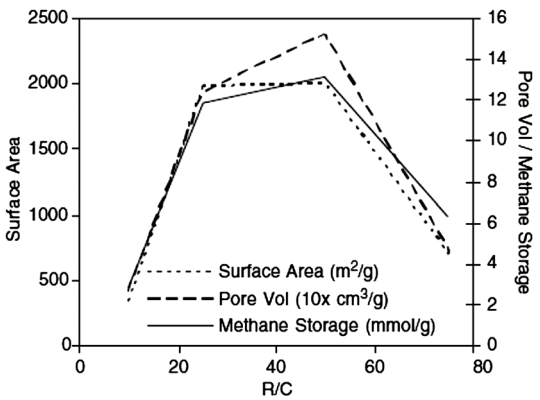

Fig. 22 Gravimetric (mmol g^{-1}) methane storage performance, surface area (m^2 g^{-1}), and total pore volume (10x cm^3 g^{-1}) as a function of R/C for carbon cryogels and activation levels from 67% to 75%.[144]

which should allow for smaller methane storage devices. However, for carbon cryogels, increased R/W improves density, but deteriorates gravimetric storage capacity. Increasing the density of the final activated carbon by increasing R/W is not an efficient way to improve the volumetric performance. The reduced gravimetric performance implies that the extra precursor/unit volume (higher R/W) is reducing in terms of its storage efficiency in the final carbon material.

The reduction in gravimetric performance may be explained in terms of the rapid gelation that was observed at high R/W. As with very high catalyst concentrations, at higher ratios of reactants to water, a limit may be reached where a significant amount of the final carbon cryogel is rendered non-porous. Once a threshold catalyst concentration is reached (this case of R/C 75 would qualify), the high R/W would enable catalyzed cross-link formation to proceed very rapidly. The close proximity of precursors to one another could result in very dense cross-linking. This may be the same effect that drove pore sizes down in the R/C experiments to the point where they might collapse and hinder the methane storage capacity of the material.

The leveling off of the density curve as R/W increases may be explained by a phenomena that was observed during gelation. During fabrication, it was noted that for materials at R/C 75 and R/W higher than 0.5, the gelation process was very fast (<10 min). A gas was formed during gelation that produced large bubbles in the gel. In a network that forms this rapidly it may be assumed that the formation of large bubbles during gelation might also indicate the presence of smaller undetectable bubbles that would cause a reduction in density. It may be possible to counter this effect by reducing the amount of catalyst to slow the reaction. Further study involving alternate R/C ratios with high R/W may lead to an ability to maintain high densities and high gravimetric methane storage capacity simultaneously.

Fig. 23b displays an increase in methane storage capacity with increased activation for R/C 75, R/W 0.25 cryogels, followed by a decline at higher activation (>70%). This improvement in storage capacity can be attributed to increased micropore volume as activation induces exposure of new micropores. The trend continues up to a point where fewer new micropores are being revealed and the average pore size begins to increase while the surface area decreases. As a result, the gas storage capacity decreases sharply with further increase in activation. As in most activated carbons, the level of activation can be used to increase the microporosity and hence storage performance of carbon cryogels, but the degree of activation does have an optimum point past which the storage performance of the material degrades due to excessive material burn off.

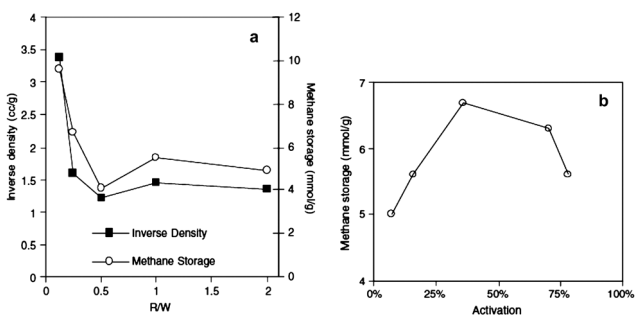

Fig. 23 (a) Gravimetric performance (mmol g^{-1}) and inverse density (cc/g) as a function of R/W on activated carbon cryogel samples with R/C of 75 and activation between 14% and 36%. (b) Methane storage performance (mmol g^{-1}) as a function of % activation for R/C 75 R/W 0.25 carbon cryogels.[144]

This study appears to be the first attempt to use carbon cryogels (or aerogels) for pressurized gas storage. The initial results are promising, but there is still considerable room for extensions of this work. Relatively few publications have reported on the properties of activated carbon aerogels.[149,150] Further understanding of this system, and possibly utilizing alternate activation temperatures, would enable better control over the final material properties.

6. Nanocomposites for hydrogen storage

It is well recognized that hydrogen generated from renewable power represents a very attractive energy solution. Hydrogen powered fuel cells are more efficient than internal combustion engines and have only water as an emission. Unfortunately, hydrogen storage systems suitable for automotive and other small-scale industrial or residential applications remain elusive. Using ultra-high pressure (860 bars) or ultra-low temperatures (30 K) continue to be the only methods for achieving sufficient and commercially practical storage densities.[151,152] This significant constraint is a well-known, yet persistent, obstacle to widespread implementation of a hydrogen economy.

Currently, a variety of solid state hydrogen storage materials are the subject of intensive investigation and research. However, no material has yet been discovered that simultaneously meets all of the following criteria:[153] relatively high storage density of 3 kWh/kg at 9 wt% and 2.7 kWh/L, moderate decomposition temperatures of 60–120 °C, good reversibility, low manufacturing cost that can support $2/kWh end-use pricing, and fast kinetics of the hydrogen absorption and desorption process. Research in solid-state hydrogen storage appears to provide the highest probability of producing a material that can satisfy these generic criteria for hydrogen storage. In this area, two families of materials hold the most promise:

Carbon-based materials: High surface area, readily accessible micropores, and extremely low weight make carbon-based materials, including activated carbon and carbon nanotubes, highly relevant. However, the low temperatures (77 K or lower) required for practical hydrogen storage densities preclude most practical applications.

Hydrides: These materials consistently demonstrate the highest theoretical capacity for hydrogen storage and many are functional at commercially relevant temperatures and pressures. Nonetheless, adoption of hydride-based storage systems is slowed by several technical obstacles. Efficient heat removal (for absorption) and heat addition (for desorption) has proven extremely difficult to achieve in metal hydride based systems.[154–156] "Overheating" and "overcooling" are typically required to overcome the inherent heat transfer barriers of hydrides. Many of the highest capacity hydrides, usually complex hydrides, have irreversible or thermodynamically demanding desorption processes.[157] Hydrides are particulate materials requiring a containment matrix for heat delivery and gas flow; such matrices have been difficult to create and maintain.

Neither carbon-based systems nor hydride systems alone have provided an adequate storage solution. As a result, despite their theoretical advantages, no solid state material has yet provided the breakthroughs required for automotive and small-scale applications.

The concept of a dual phase coherent nanocomposite hydrogen storage material has been developed and studied, where the two phases consist of highly porous carbon and hydride hydrogen storage material.[55,158–161] Porous carbon with a high surface area and pore volume would contribute significantly to a solid state hydride-based hydrogen storage composite material by providing a structural support matrix, as well as size confinement for hydrides and a percolated heat conduction network. Fig. 24 is a schematic illustrating the coherent complex hydride - ammonia borane (AB) nanocomposite that was chosen as a hydride material for its high gravimetric and volumetric hydrogen content, as well as its already reasonable decomposition temperature. AB is also easily coated onto the carbon cryogel by dissolving it in solvent and soaking the cryogel, resulting in a coherent nanocomposite, as illustrated in Fig. 25. The addition of AB to the carbon cryogel resulted in hydrogen release at a much lower temperature and the elimination of harmful byproducts.

Carbon cryogel (CC) – ammonia borane (AB) nanocomposites can be made by loading monolithic CCs with AB through soaking them in AB/THF solution (Fig. 25);[162,163] the total weight gain of the samples are between 30–50wt% (1 : 2–1 : 1 by weight ratio for AB:CC). Nitrogen sorption analysis is used to study the porous structure of CCs and CC-ABs, and it is shown that the CC samples are mesoporous with pore sizes of 2–50nm. The specific surface areas of CCs and CC-ABs are 350–500 m^2 g^{-1}, and their total pore volumes are 0.7–0.97 cm^3 g^{-1}. The pore size distributions can be obtained by applying the BJH method on the desorption curve of the isotherms.[71] Fig. 26a shows the distributions of three CC samples with pore diameters centered at ~7, 9 and 16nm. Fig. 26b shows the changes in the pore size distribution of the 7nm-CC when loaded with AB (CC-AB), and after dehydrogenation (reacted). Loading CCs with AB fills some of the mesopores, resulting in an appreciable reduction in pore volume and a shift in the pore size distribution toward smaller pore sizes (7.5 nm → 6.5 nm). This can be indicative of uniform loading of AB throughout the CCs. The porous structure of the CC is maintained after thermal reaction; dehydrogenation partially emptied some of the filled pores and increased pore volume, but the pore size distribution did not show an appreciable shift.

The DSC exotherms for CC-ABs and neat AB are given in Fig. 27. Thermal decomposition of neat AB happens through two step reactions, which were observed at approximately 115 and 150 °C at the applied heating rate. These temperatures are in good agreement with the literature.[164] Similar results were reported in other nanocomposites, including mesoporous silica-AB[165] and carbon aerogel-$LiBH_4$.[166] For the CC-AB nanocomposites, dehydrogenation temperatures are much lower than that of neat AB and hydrogen release happens through only one exothermic event. For the CCs with pore sizes of 7, 9 and 16 nm, dehydrogenation temperatures are at ~98, 102 and 110 °C, respectively. Lower dehydrogenation temperatures in CC-ABs provide evidence of faster kinetics. The dehydrogenation of

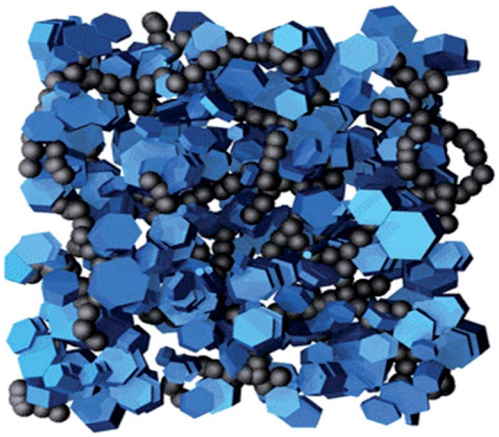

Fig. 24 Illustration of the anticipated structure of a coherent nanocomposite consisting of a carbon cryogel network and hydride.[162]

nanocomposites is very reproducible and results in the release of about 1.5 H_2 equiv and suppression of borazine. Also, the reaction exothermicity is significantly more than that of neat AB.[162] A previous study using ^{11}B nuclear magnetic resonance and FTIR showed the lower dehydrogenation temperature and enhanced kinetics in the thermal reaction of CC-AB is accompanied by the formation of a new reaction product, which is attributed to the reaction of AB with surface oxygen functional groups.[167] It should also be noted the dehydrogenation occurred at a much narrower range of temperatures. Although the exact mechanism for narrowed dehydrogenation peaks is still under research, it is likely due to the better thermal conductivity of the nanocomposites and the consequent rapid kinetics as compared to the neat AB. The peak dehydrogenation of CC-ABs and their corresponding CC pore size are compared in Fig. 27b, which reveals that the dehydrogenation temperature decreases almost linearly with pore size.

Activation energies are calculated for non-isothermal DSC runs using the Kissinger equation,[168] given by:

$$\ln(\alpha/T_p^2) = -E_a/RT_p + C \quad (5)$$

where T_p is the peak temperature, $\alpha = dT/dt$ is the heating rate, E_a is the activation energy, and C is the intercept. The plot of ln

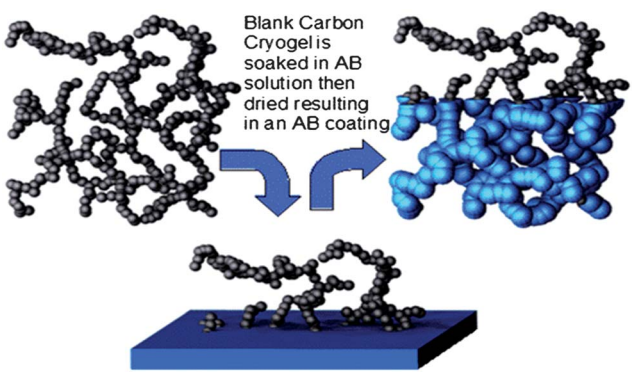

Fig. 25 Schematic of preparation of carbon cryogels (CC) – ammonia borane (AB) nanocomposites.

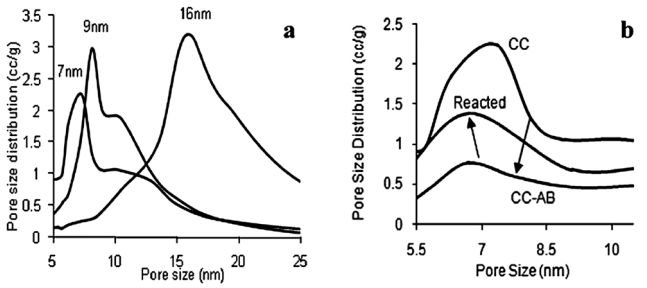

Fig. 26 (a) Pore size distribution of CCs used for making CC-AB nanocomposites, as determined by the BJH method from the desorption curves of nitrogen sorption isotherms, and (b) pore size distribution of the 7 nm CC and CC-AB nanocomposite before and after dehydrogenation.[163]

(α/T_p^2) *versus* $1/T_p$ is linear and the slope of the resulting line corresponds to the values of the activation energy from the Kissinger equation. Table 1 shows the peak temperatures for heating rates of 2, 5, and 10 °C min^{-1}. The calculated activation energy for neat AB is about 160 kJ mol^{-1}, which is comparable to the value reported in literature using the isothermal method.[165] The activation energies for nanocomposites are lower than that of neat AB: about 150 kJ mol^{-1} AB and 120 kJ mol^{-1} AB for 16nm-CC-AB, and 7nm-CC-AB, respectively. Similar to the dehydrogenation temperatures, the activation energies decrease with decreasing pore size. These results suggest that the barrier for hydrogen release from CC-ABs is lower than that of the neat AB.

The dehydrogenation temperature and kinetics of ammonia borane on pore size in amorphous nanoporous carbon –ammonia borane nanocomposites vary appreciably with the change in pore size of the CC scaffold. Confining nanocrystallite AB inside the mesopores of the carbon matrix decreases the dehydrogenation temperatures and activation energy. The carbon matrix reduces hydrogen diffusion distances, increases the frequency of reaction, which effectively accelerates the dehydrogenation process, and serves as efficient pathways for heat transfer. Inside the mesopores of the CC matrix, nanocrystallite AB possesses a huge surface to volume ratio, resulting in significantly larger surface energy. This destabilizes the hydrogen bonding network of AB and lowers the barrier to hydrogen release. Other possible factors, such as surface area and catalysts, on dehydrogenation temperatures and the kinetics of hydrides have also been studied; boron and nitrogen modified CCs have shown to enhance kinetics and lower dehydrogenation temperatures further.

Fig. 28 shows the DSC exotherms (at 5 °C min^{-1}) for AB, CC-AB, and BNCC-AB nanocomposites. Thermal decomposition of AB shows an endothermic dip at approximately 105 °C (assigned to the melting of AB) and two exothermic maxima, one at approximately 115 °C and a smaller one ~150 °C, associated with the release of the first and second equivalent of hydrogen, respectively. These observations are in good agreement with the literature.[164,169] However, the DSC exotherms for CC-AB and BNCC-AB show two notable differences as compared to neat AB. First, the temperature for hydrogen release is lower (~109 °C for CC-AB and ~103 °C for BNCC-AB, compared to 118 °C for AB). Also, there is only one exothermic event and no other peak is observed at temperatures as high as 160 °C. The activation energy for release of the first equivalent of hydrogen from neat AB is found to be ~160 kJ mol^{-1}, which is comparable to the value reported in literature.[170] The activation energies for nancomposites are ~150 kJ mol^{-1} AB and 115 kJ mol^{-1} AB for CC-AB and BNCC-AB, respectively.

The lower dehydrogenation temperatures and activation energies of CC-AB and BNCC-AB can be attributed to the size dependent surface energy of AB confined inside the nanoscale pores of CC and BNCC. The carbon matrix can reduce hydrogen diffusion distances, increase the frequency of reaction, which effectively accelerates the dehydrogenation process, and serve as efficient pathways for heat transfer. Thus, the barrier to hydrogen release in CC-AB and BNCC-AB is lower. Also, the surface hydroxyl groups may result in the catalysis of the AB thermal reaction in nanocomposites. Furthermore, the lower activation energy and dehydrogenation temperature in BNCC-AB than that of CC-AB can be attributed to the catalytic effect and not the nanoscale effects. The presence of B, N, and the excess of hydroxyl groups on the surface BNCC can provide surface interactions that disrupt the dihydrogen bonding in AB. Therefore, the induction period for dehydrogenation is lower,

Table 1 Peak temperatures for dehydrogenation of AB and CC-AB[163]

Heating rate (°C min^{-1})	AB T_p (°C)	16 nm CC-AB T_p (°C)	7 nm CC-AB T_p (°C)
10	124	115	109
5	118	109	101
2	112	103	94
E_a	**160 kJ mol^{-1}**	**150 kJ mol^{-1}**	**120 kJ mol^{-1}**

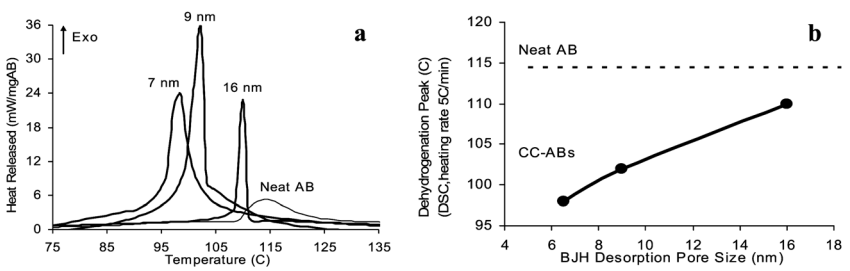

Fig. 27 (a) DSC exotherms for CC-AB nanocomposites at a heating rate of 5 °C min^{-1} and (b) comparison of dehydrogenation peaks for CC-AB nanocomposites for corresponding CC pore sizes. The dashed line shows the dehydrogenation temperature for AB at a similar heating rate.[163]

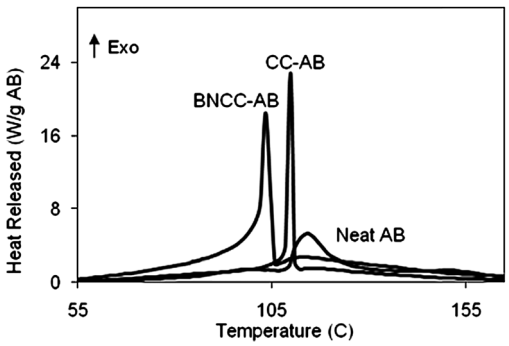

Fig. 28 DSC exotherms for CC-AB and BNCC-AB nanocomposites and neat AB (heating rate 5 °C min^{-1}).[78]

resulting in a lower barrier to hydrogen release in BNCC-AB as compared to CC-AB.

7. Summary

Sol–gel processing is a versatile chemical synthesis route for the fabrication of highly porous amorphous graphitic carbon. The porous structure and bulk chemistry of the resulting carbon can be tuned through the selection of precursors, catalysts, and solvents, as well as the processing conditions. The surface chemistry and porous structure of carbon can be further manipulated through solvent exchange or chemical impregnation, controlled removal of the solvent, pyrolysis, and activation. With controlled chemistry and porous structure, highly porous carbons demonstrated excellent properties for energy related applications. Carbon cryogels with tuned porous structure and surface chemistry offered higher specific capacity, better cyclic stability, and potentially higher working voltage when used as electrodes for supercapacitors. It was also demonstrated that carbon cryogels are a viable media for natural gas storage at reduced pressure. When used as matrices, carbon cryogels make it possible to fully utilize transition metal oxides as cathodic materials for lithium ion intercalation with enhanced specific power. When hydrides are confined inside pores of highly porous carbon to form coherent nanocomposites, the dehydrogenation temperatures and reaction pathways are both changed significantly: the dehydrogenation temperature and activation energy decrease with a reducing pore size, and also change with the surface chemistry of porous carbon.

Acknowledgements

This work has been supported in part by the National Science Foundation (DMI-0455994, DMR-0605159, and CMMI-1030048) and Air Force Office of Scientific Research (AFOSR-MURI, FA9550-06-1-0326). This work has also been supported by Washington Technology Center, Pacific Northwest National Laboratories (PNNL), Intel Labs, National Center for Nanomaterials Technology (Postech, Korea) and EnerG2. SLC acknowledges the University of Washington Bioenergy IGERT fellowship (DGE-0654252) and the GO-MAP fellowship.

References

1 H. O. Pierson, *Handbook of Carbon, Graphite, Diamond and Fullerenes*, Noyes Publications, Park Ridge, NJ 1993.
2 S. R. P. Silva, *Properties of Amorphous Carbon*, INSPEC, London 2003.
3 B. C. Thompson and J. M. J. Frechet, *Angew. Chem., Int. Ed.*, 2008, **47**, 58–77.
4 S. H. Park, A. Roy, S. Beaupre, S. Cho, N. Coates, J. S. Moon, D. Moses, M. Leclerc, K. Lee and A. J. Heeger, *Nat. Photonics*, 2009, **3**, 297–U5.
5 H. Spanggaard and F. C. Krebs, *Sol. Energy Mater. Sol. Cells*, 2004, **83**, 125–146.
6 G. Dennler, M. Scharber and C. J. Brabec, *Adv. Mater.*, 2009, **21**, 1323–1338.
7 A. D. Pasquier, H. E. Unalan, A. Kanwal, S. Miller and M. Chhowalla, *Appl. Phys. Lett.*, 2005, **87**, 203511.
8 Y. K. Kim and D. H. Min, *Langmuir*, 2009, **25**, 11302–11306.
9 D. S. Hecht, L. B. Hu and G. Irvin, *Adv. Mater.*, 2011, **23**, 1482–1513.
10 Y. Q. Sun, Q. O. Wu and G. Q. Shi, *Energy Environ. Sci.*, 2011, **4**, 1113–1132.
11 L. L. Zhang, R. Zhou and X. S. Zhao, *J. Mater. Chem.*, 2010, **20**, 5983–5992.
12 S. R. C. Vivekchand, C. S. Rout, K. S. Subrahmanyam, A. Govindaraj and C. N. R. Rao, *J. Chem. Sci.*, 2008, **120**, 9–13.
13 K. S. Subrahmanyam, S. R. C. Vivekchand, A. Govindaraj and C. N. R. Rao, *J. Mater. Chem.*, 2008, **18**, 1517–1523.
14 E. Frackowiak and F. Beguin, *Carbon*, 2002, **40**, 1775–1787.
15 E. Yoo, J. Kim, E. Hosono, H. Zhou, T. Kudo and I. Honma, *Nano Lett.*, 2008, **8**, 2277–2282.
16 Y. P. Wu, E. Rahm and R. Holze, *J. Power Sources*, 2003, **114**, 228–236.
17 B. J. Landi, M. J. Ganter, C. D. Cress, R. A. DiLeo and R. P. Raffaelle, *Energy Environ. Sci.*, 2009, **2**, 638–654.
18 T. Otowa, Y. Nojima and T. Miyazaki, *Carbon*, 1997, **35**, 1315–1319.
19 C. Y. Lu and H. S. Chiu, *Chem. Eng. Sci.*, 2006, **61**, 1138–1145.
20 V. Gomez-Serrano, A. Macias-Garcia, A. Espinosa-Mansilla and C. Valenzuela-Calahorro, *Water Res.*, 1998, **32**, 1–4.
21 M. C. Annesini, C. Di Carlo, V. Piemonte and L. Turchetti, *Biochem. Eng. J.*, 2008, **40**, 205–210.
22 D. J. Malik, G. L. Warwick, I. Mathieson, N. A. Hoenich and M. Streat, *Carbon*, 2005, **43**, 2317–2329.
23 R. J. A. Bigsby, R. J. Rider and G. N. Blount, *Proc. Inst. Mech. Eng., Part H*, 1998, **212**, 373–381.
24 C. Ye, Q. M. Gong, F. P. Lu and J. Liang, *Sep. Purif. Technol.*, 2007, **58**, 2–6.
25 S. H. Joo, S. J. Choi, I. Oh, J. Kwak, Z. Liu, O. Terasaki and R. Ryoo, *Nature*, 2001, **412**, 169–172.
26 E. Auer, A. Freund, J. Pietsch and T. Tacke, *Appl. Catal., A*, 1998, **173**, 259–271.
27 G. G. Park, T. H. Yang, Y. G. Yoon, W. Y. Lee and C. S. Kim, *Int. J. Hydrogen Energy*, 2003, **28**, 645–650.
28 A. Guha, W. J. Lu, T. A. Zawodzinski and D. A. Schiraldi, *Carbon*, 2007, **45**, 1506–1517.
29 A. Ahmadpour and D. D. Do, *Carbon*, 1996, **34**, 471–479.
30 M. Jagtoyen and F. Derbyshire, *Carbon*, 1998, **36**, 1085–1097.
31 Z. H. Hu and M. P. Srinivasan, *Microporous Mesoporous Mater.*, 1999, **27**, 11–18.
32 A. Aygun, S. Yenisoy-Karakas and I. Duman, *Microporous Mesoporous Mater.*, 2003, **66**, 189–195.
33 M. Ahmedna, W. E. Marshall and R. M. Rao, *Bioresour. Technol.*, 2000, **71**, 113–123.
34 R. W. Pekala, *J. Mater. Sci.*, 1989, **24**, 3221–3227.
35 R. W. Pekala and F. M. Kong, *Polym. Prepr.*, 1989, **30**, 221–223.
36 H. Tamon, H. Ishizaka, T. Yamamoto and T. Suzuki, *Carbon*, 1999, **37**, 2049–2055.
37 D. C. Wu, R. W. Fu, S. T. Zhang, M. S. Dresselhaus and G. Dresselhaus, *J. Non-Cryst. Solids*, 2004, **336**, 26–31.
38 D. Kawashima, T. Aihara, Y. Kobayashi, T. Kyotani and A. Tomita, *Chem. Mater.*, 2000, **12**, 3397–3401.
39 N. Job, R. Pirard, J. Marien and J. P. Pirard, *Carbon*, 2004, **42**, 619–628.
40 C. Lin and J. A. Ritter, *Carbon*, 1997, **35**, 1271–1278.

41 Y. Gogotsi, A. Nikitin, H. H. Ye, W. Zhou, J. E. Fischer, B. Yi and H. C. Foley, *Nat. Mater.*, 2003, **2**, 591–594.
42 R. Dash, J. Chmiola, G. Yushin, Y. Gogotsi, G. Laudisio, J. Singer, J. Fischer and S. Kucheyev, *Carbon*, 2006, **44**, 2489–2497.
43 E. Kockrick, C. Schrage, L. Borchardt, N. Klein, M. Rose, I. Senkovska and S. Kaskel, *Carbon*, 2010, **48**, 1707–1717.
44 J. S. Beck, J. C. Vartuli, W. J. Roth, M. E. Leonowicz, C. T. Kresge, K. D. Schmitt, C. T. W. Chu, D. H. Olson, E. W. Sheppard, S. B. McCullen, J. Higinns and J. L. Schlenker, *J. Am. Chem. Soc.*, 1992, **114**, 10834–10843.
45 J. Lee, J. Kim and T. Hyeon, *Adv. Mater.*, 2006, **18**, 2073–2094.
46 R. Ryoo, S. H. Joo and S. Jun, *J. Phys. Chem. B*, 1999, **103**, 7743–7746.
47 J. Lee, S. Yoon, T. Hyeon, S. M. Oh and K. B. Kim, *Chem. Commun.*, 1999, 2177–2178.
48 C. J. Brinker and G. W. Scherer, *Sol–Gel Science: The Physics and Chemistry of Sol–Gel Processing*, Academic Press, San Diego, CA 1990.
49 A. C. Pierre, *Introduction to Sol–Gel Processing*, Kluwer, Norwell, MA 1998.
50 H. M. Shang, Y. Wang, M. Bliss and G. Z. Cao, *Appl. Phys. Lett.*, 2005, **87**, 051909.
51 T. P. Chou, Q. F. Zhang, G. E. Fryxell, B. Russo and G. Z. Cao, *J. Phys. Chem. C*, 2007, **111**, 6296–6302.
52 Q. F. Zhang and G. Z. Cao, *Nano Today*, 2011, **6**, 91–109.
53 A. C. Pierre and G. M. Pajonk, *Chem. Rev.*, 2002, **102**, 4243–4266.
54 K. Barral, *J. Non-Cryst. Solids*, 1998, **225**, 46–50.
55 J. Biener, M. Stadermann, M. Suss, M. A. Worsley, M. M. Biener, K. A. Rose and T. F. Baumann, *Energy Environ. Sci.*, 2011, **4**, 656–667.
56 C. Moreno-Castilla, M. B. Dawidziuk, F. Carrasco-Marin and Z. Zapata-Benabithe, *Carbon*, 2011, **49**, 3808–3819.
57 J. Z. Feng, J. Feng and C. R. Zhang, *J. Sol-Gel Sci. Technol.*, 2011, **59**, 371–380.
58 S. Tsujimura, A. Nishina, Y. Hamano, K. Kano and S. Shiraishi, *Electrochem. Commun.*, 2010, **12**, 446–449.
59 C. Liu, F. Li, L. P. Ma and H. M. Cheng, *Adv. Mater.*, 2010, **22**, E28–E62.
60 S. W. Lee, B. M. Gallant, H. R. Byon, P. T. Hammond and Y. Shao-Horn, *Energy Environ. Sci.*, 2011, **4**, 1972–1985.
61 P. J. Hall, M. Mirzaeian, S. I. Fletcher, F. B. Sillars, A. J. Rennie, G. O. Shitta-Bey, G. Wilson, A. Cruden and R. Carter, *Energy Environ. Sci.*, 2010, **3**, 1238–1251.
62 S. L. Candelaria, Y. Y. Shao, Y. Zhou, X. L. Li, J. Xiao, J. Zhang, J. Zhang, Y. Wang, J. Liu, J. H. Li and G. Z. Cao, *Nano Energy*, 2011, submitted for publication.
63 E. Frackowiak, *J. Braz. Chem. Soc.*, 2006, **17**, 1074–1082.
64 S. A. Al-Muhtaseb and J. A. Ritter, *Adv. Mater.*, 2003, **15**, 101–114.
65 B. B. Garcia, D. W. Liu, S. Sepehri and G. Z. Cao, *J. Non-Cryst. Solids*, 2010, **356**, 1620–1625.
66 J. Stöhr, *NEXAFS Spectroscopy*, Springer-Verlag, Berlin 1992.
67 W. Daud, W. S. W. Ali and M. Z. Sulaiman, *J. Chem. Technol. Biotechnol.*, 2003, **78**, 1–5.
68 B. B. Garcia, A. M. Feaver, Q. Zhang, R. D. Champion, G. Z. Cao, T. T. Fister, K. P. Nagle and G. T. Seidler, *J. Appl. Phys.*, 2008, **104**, 014305–014309.
69 H. F. Stoeckli, *Carbon*, 1990, **28**, 1–6.
70 E. P. Barrett, L. G. Joyner and P. P. Halenda, *J. Am. Chem. Soc.*, 1951, **73**, 372–380.
71 G. Q. Lu and X. S. Zhao, *Nanoporous Materials: Science and Engineering*, Imperial College Press, London 2004.
72 A. Braun, M. Bartsch, B. Schnyder, R. Kotz, O. Haas and A. Wokaun, *Carbon*, 2002, **40**, 375–382.
73 S. Blazewicz, A. Swiatkowski and B. J. Trznadel, *Carbon*, 1999, **37**, 693–700.
74 B. B. Garcia, S. L. Candelaria and G. Z. Cao, *Renewable Energy*, 2011, **36**, 1788–1794.
75 H. Y. Tian, C. E. Buckley, S. Mule, M. Paskevicius and B. B. Dhal, *Nanotechnology*, 2008, **19**, 475605.
76 X. Zhang, M. Looney, D. Solomon and A. Whittaker, *Polymer*, 1997, **38**, 5835–5848.
77 X. Zhang and D. Solomon, *Chem. Mater.*, 1999, **11**, 384–391.
78 S. Sepehri, B. B. García and G. Z. Cao, *Eur. J. Inorg. Chem.*, 2009, 599–603.
79 S. Sepehri, B. B. García, Q. F. Zhang and G. Z. Cao, *Carbon*, 2009, **47**, 1436–1443.
80 K. Jurewicz, K. Babel, A. Ziolkowski and H. Wachowska, *Electrochim. Acta*, 2003, **48**, 1491–1498.
81 D. Hulicova-Jurcakova, M. Kodama, S. Shiraishi, H. Hatori, Z. H. Zhu and G. Q. Lu, *Adv. Funct. Mater.*, 2009, **19**, 1800–1809.
82 E. Frackowiak and F. Beguin, *Carbon*, 2001, **39**, 937–950.
83 W. C. Chen, T. C. Wen and H. Teng, *Electrochim. Acta*, 2003, **48**, 641–649.
84 Z. Lei, Z. Chen and X. S. Zhao, *J. Phys. Chem. C*, 2010, **114**, 19867–19874.
85 M. Wu, G. A. Snook, V. Gupta, M. Shaffer, D. J. Fray and G. Z. Chen, *J. Mater. Chem.*, 2005, **15**, 2297–2302.
86 M. Kawaguchi, A. Itoh, S. Yagi and H. Oda, *J. Power Sources*, 2007, **172**, 481–486.
87 F. Ullmann, W. Gerhartz, Y. S. Yamamoto, F. T. Campbell, R. Pfefferkorn and J. F. Rounsaville, *Ullmann's Encyclopedia of Industrial Chemisty*, VCH, Deerfield Beach, Florida, U.S.A. 2007.
88 J. Jiang, Q. Gao, K. Xia and J. Hu, *Microporous Mesoporous Mater.*, 2009, **118**, 28–34.
89 W. Li, D. Chen, Z. Li, Y. Shi, Y. Wan, G. Wang, Z. Jiang and D. Zhao, *Carbon*, 2007, **45**, 1757–1763.
90 W. Kim, M. Y. Kang, J. B. Joo, N. D. Kim, I. K. Song, P. Kim, J. R. Yoon and J. Yi, *J. Power Sources*, 2010, **195**, 2125–2129.
91 G. Lota, K. Lota and E. Frackowiak, *Electrochem. Commun.*, 2007, **9**, 1828–1832.
92 http://www.hybridcars.com/make/honda-mpg, accessed 7 September 2011.
93 http://afstrinity.com, accessed 7 September 2011.
94 http://www.edncom/contents/images/ec22ss.pdf, accessed 7 September 2011.
95 A. F. Burke, *Proc. IEEE*, 2007, **95**, 806–820.
96 V. V. N. Obreja, *Phys. E.*, 2008, **40**, 2596–2605.
97 B. E. Conway, *Electrochemical Supercapacitors Scientific Fundamentals and Technological Applications*, Plenum Press, New York 1999.
98 W. Feng and X. Bin, *New Carbon Mater.*, 2006, **21**, 176–184.
99 A. Garcia-Gomez, P. Miles, T. A. Centeno and J. M. Rojo, *Electrochim. Acta*, 2010, **55**, 8539–8544.
100 E. G. Calvo, C. O. Ania, L. Zubizarreta, J. A. Menendez and A. Arenillas, *Energy Fuels*, 2010, **24**, 3334–3339.
101 A. Szczurek, K. Jurewicz, G. Amaral-Labat, V. Fierro, A. Pizzi and A. Celzard, *Carbon*, 2010, **48**, 3874–3883.
102 M. Inagaki, H. Konno and O. Tanaike, *J. Power Sources*, 2010, **195**, 7880–7903.
103 M. Kodama, J. Yamashita, Y. Soneda, H. Hatori, S. Nishimura and K. Kamegawa, *Mater. Sci. Eng., B*, 2004, **108**, 156–161.
104 D. Hulicova, J. Yamashita, Y. Soneda, H. Hatori and M. Kodama, *Chem. Mater.*, 2005, **17**, 1241–1247.
105 T. Yamamoto, T. Nishimura, T. Suzuki and H. Tamon, *J. Non-Cryst. Solids*, 2001, **288**, 46–55.
106 J. G. Lee, J. Y. Kim and S. H. Kim, *J. Power Sources*, 2006, **160**, 1495–1500.
107 T. E. Rufford, D. Hulicova-Jurcakova, Z. Zhu and G. Q. Lu, *Electrochem. Commun.*, 2008, **10**, 1594–1597.
108 H. A. Andreas, K. Lussier and A. M. Oickle, *J. Power Sources*, 2009, **187**, 275–283.
109 C. O. Ania, V. Khomenko, E. Raymundo-Pinero, J. B. Parra and F. Beguin, *Adv. Funct. Mater.*, 2007, **17**, 1828–1836.
110 G. Lota, B. Grzyb, H. Machnikowska, J. Machnikowska and E. Frackowiak, *Chem. Phys. Lett.*, 2005, **404**, 53–58.
111 E. Frackowiak, *Phys. Chem. Chem. Phys.*, 2007, **9**, 1774–1785.
112 P. Azais, L. Duclaux, P. Florian, D. Massiot, M. A. Lillo-Rodenas, A. Linares-Solano, J. P. Peres, C. Jehoulet and F. Beguin, *J. Power Sources*, 2007, **171**, 1046–1053.
113 J. M. Tarascon and M. Armand, *Nature*, 2001, **414**, 359–367.
114 J. Hassoun, P. Reale and B. Scrosati, *J. Mater. Chem.*, 2007, **17**, 3668–3677.
115 M. Armand and J. M. Tarascon, *Nature*, 2008, **451**, 652–357.
116 L. Taberna, S. Mitra, P. Poizot, P. Simon and J. M. Tarascon, *Nat. Mater.*, 2006, **5**, 567–573.
117 E. A. Ponzio, T. M. Benedetti and R. M. Torresi, *Electrochim. Acta*, 2007, **52**, 4419–4427.
118 Y. Wang and G. Z. Cao, *Adv. Mater.*, 2008, **20**, 2251–2269.

119 Y. Wang, K. Takahashi, K. Lee and G. Z. Cao, *Adv. Funct. Mater.*, 2006, **16**, 1133–1144.
120 T. Watanabe, Y. Ikeda, T. Ono, M. Hibino, M. Hosoda, K. Sakai and T. Kudo, *Solid State Ionics*, 2002, **151**, 313–320.
121 I. Boyano, M. Bengoechea, I. de Meatza, O. Miguel, I. Cantero, E. Ochoteco, J. Rodriguez, M. Lira-Cantu and P. Gomez-Romero, *J. Power Sources*, 2007, **166**, 471–477.
122 L. Li and Z. F. Yan, *Stud. Surf. Sci. Catal.*, 2005, **156**, 523–528.
123 K. Takahashi, Y. Wang and G. Z. Cao, *J. Phys. Chem. B*, 2005, **109**, 48–51.
124 A. Q. Pan, D. W. Liu, X. Y. Zhou, B. B. Garcia, S. Q. Liang and G. Z. Cao, *J. Power Sources*, 2010, **195**, 3893–3899.
125 E. Potiron, A. L. La Salle, A. Verbaere, Y. Piffard and D. Guyomard, *Electrochim. Acta*, 1999, **45**, 197–214.
126 R. J. Al-Muhtaseb and J. A. Ritter, *Adv. Mater.*, 2003, **15**, 101–114.
127 S. Passerini, J. J. Ressler, D. B. Le, B. B. Owens and W. H. Smyrl, *Electrochim. Acta*, 1999, **44**, 2209–2217.
128 I. H. Kim, J. H. Kim, B. W. Cho, Y. H. Lee and K. B. Kim, *J. Electrochem. Soc.*, 2006, **153**, A989–A996.
129 D. W. Liu, B. B. Garcia, Q. Zhang, Q. Guo, Y. H. Zhang, S. Sepehri and G. Z. Cao, *Adv. Funct. Mater.*, 2009, **19**, 1015–1023.
130 D. W. Liu, Y. Liu, B. B. Garcia, Q. Zheng, A. Q. Pan, Y. H. Jeong and G. Z. Cao, *J. Mater. Chem.*, 2009, **19**, 8789–8795.
131 J. Liu, G. Z. Cao, Z. G. Yang, D. H. Wang, D. Dubois, X. D. Zhou, G. L. Graff, L. R. Pederson and J. G. Zhang, *ChemSusChem*, 2008, **1**, 676–697.
132 http://www.ngvc.org/about_ngv/index.html, accessed 7 September 2011.
133 E. Kennedy, The Fresno Bee, 2 April 2005, B1.
134 J. T. Eberhardt, *2002 Diesel Engine Emissions Reduction (DEER) Workshop*, 25–29 Aug 2002, San Diego, CA.
135 S. Biloe, V. Goetz and A. Guillot, *Carbon*, 2002, **40**, 1295–1308.
136 T. Duren, L. Sarkisov, O. M. Yaghi and R. Q. Snurr, *Langmuir*, 2004, **20**, 2683–2689.
137 A. Perrin, A. Celzard, J. F. Mareche and G. Furdin, *Energy Fuels*, 2003, **17**, 1283–1291.
138 A. C. Lua and T. Yang, *Carbon*, 2004, **42**, 219–238.
139 T. Yang and A. C. Lua, *Microporous Mesoporous Mater.*, 2003, **63**, 113–124.
140 A. C. Lua and T. Yang, *J. Colloid Interface Sci.*, 2004, **274**, 594–601.
141 A. C. Lua, T. Yang and J. Guo, *J. Anal. Appl. Pyrolysis*, 2004, **72**, 279–287.
142 J. Alcaniz-Monge, M. A. De La Casa-Lillo, C. Cazorla-Amoros and A. Linares-Solano, *Carbon*, 1997, **35**, 291–297.
143 T. A. Brady, M. Rostam-Abadi and M. J. Rood, *Gas Sep. Purif.*, 1996, **10**, 97–102.
144 A. M. Feaver and G. Z. Cao, *Carbon*, 2006, **44**, 590–593.
145 Y. S. Hsu and T. P. Perng, *J. Alloys Compd.*, 1995, **227**, 180–185.
146 K. Imomata, K. Kanazawa, Y. Urabe, H. Hosono and T. Araki, *Carbon*, 2002, **40**, 87–93.
147 R. W. Pekala, *Macromolecules*, 1993, **26**, 5487–5493.
148 H. Tamon, H. Ishizaka, M. Mikami and M. Okazaki, *Carbon*, 1997, **35**, 791–796.
149 B. Fang, Y. Z. Wei, K. Maruyama and M. Kumagai, *J. Appl. Electrochem.*, 2005, **35**, 229–233.
150 C. Schmitt, H. Probstle and J. Fricke, *J. Non-Cryst. Solids*, 2001, **285**, 277–282.
151 V. P. Utgikar, *Technol. Soc.*, 2005, **27**, 315–320.
152 J. F. Hake, J. Lissen and M. Walbeck, *Energy Policy*, 2006, **34**, 1271–1283.
153 W. Grochala and P. P. Edwards, *Chem. Rev.*, 2004, **104**, 1283–1315.
154 Y. Asakuma, S. Miyauchi, T. Yamamoto, H. Aoki and T. Miura, *Int. J. Hydrogen Energy*, 2003, **28**, 529–536.
155 T. Nakagawa, A. Inomata, H. Aoki and T. Miura, *Int. J. Hydrogen Energy*, 2000, **25**, 339–350.
156 J. Bloch and M. H. Mintz, *J. Alloys Compd.*, 1997, **253–254**, 529–541.
157 H. K. Birnbaumn, C. Buckley, F. Ziedes, E. Sirois, P. Rozenak, S. Sponner and J. S. Lin, *J. Alloys Compd.*, 1997, **253–254**, 260–264.
158 A. F. Gross, C. C. Ahn, S. L. Van Atta, P. Liu and J. J. Vajo, *Nanotechnology*, 2009, **20**, 204005.
159 C. Z. Wu and H. M. Cheng, *J. Mater. Chem.*, 2010, **20**, 5390–5400.
160 S. Cahen, J. B. Eymery and R. Janot, *J. Power Sources*, 2009, **189**, 902–908.
161 L. Li, X. Yao, C. H. Sun, A. J. Du, L. N. Cheng, Z. H. Zhu, C. Z. Yu, J. Zou, S. C. Smith, P. Wang, H. M. Cheng, R. L. Frost and G. Q. M. Lu, *Adv. Funct. Mater.*, 2009, **19**, 265–271.
162 A. M. Feaver, S. Sepehri, P. Shamberger, A. Stowe, T. Autrey and G. Z. Cao, *J. Phys. Chem. B*, 2007, **111**, 7469–7472.
163 S. Sepehri, B. B. Garcia and G. Z. Cao, *J. Mater. Chem.*, 2008, **18**, 4034–4037.
164 F. Baitalow, J. Baumann, G. Wolf, K. Jaenicke-Röβler and G. Leitner, *Thermochim. Acta*, 2002, **391**, 159–168.
165 A. Gutowska, L. Li, Y. Shin, C. M. Wang, X. H. S. Li, J. C. Linehan, R. S. Smith, B. D. Kay, B. Schmid, W. Shaw, M. Gutowski and T. Autrey, *Angew. Chem., Int. Ed.*, 2005, **44**, 3578–3582.
166 A. F. Gross, J. J. Vajo, S. L. Van Atta and G. L. Olson, *J. Phys. Chem. C*, 2008, **112**, 5651–5657.
167 S. Sepehri, A. M. Feaver, W. J. Shaw, C. J. Howard, Q. Zhang, T. Autrey and G. Z. Cao, *J. Phys. Chem. B*, 2007, **111**, 14285–14289.
168 H. E. Kissinger, *Anal. Chem.*, 1957, **29**, 1702–1706.
169 T. B. Marder, *Angew. Chem., Int. Ed.*, 2007, **46**, 8116–8118.
170 F. H. Stephens, V. Pons and R. T. Baker, *Dalton Trans.*, 2007, 2613–2626.